The University Of Queensland
AUSTRALIA

Two dimensional vortex phenomena in a Bose-Einstein Condensate

Kwan Goddard Lee
BSc/BMath

Under the supervision of
Dr Tyler Neely, Dr Matthew Reeves

A thesis submitted to the University of Queensland
in partial fulfilment of the degree of Bachelor of Science with Honours
School of School of Maths and Physics
June 2019

Examiner's Copy

© Kwan Goddard Lee, 2019.

Typeset in $\LaTeX\,2_\varepsilon$.

The work presented in this Thesis is, to the best of my knowledge and belief original, except as acknowledged in the text, and has not been submitted either in whole or in part, for a degree at this or any other university.

Kwan Goddard Lee

Abstract

The recent development of configurable optical trapping techniques for dilute atomic Bose-Einstein condensates, a macroscopically occupied quantum state and hence a superfluid, allow highly controllable experiments. The UQ BEC lab is capable of creating highly oblate BECs, ideal for experiments on two dimensional vortex dynamics. In this thesis, we present two experimental studies of the dynamics of these point vortices. In 1949 Lars Onsager predicated that point vortices in a bounded fluid must cluster at high energies, at a negative thermodynamic temperature. This was a very influential theory, explaining the stability of large two dimensional vortices, such as the Great Red Spot on Jupiter. The first section of this thesis investigates a system of same-signed vortices, known as the chiral system. This is predicted to have on-axis vortex equilibrium states at low energy, with a symmetry breaking transition to off-axis vortex clusters at high energies. We present the first observations of these equilibrium states, as well as the relaxation of a non-equilibrium state into an off-axis cluster. The data is very well described by our numerical calculations. These results answer some previously open theoretical questions such the relaxation time of vortices into equilibrium. The second experiment involves the dynamics of bound vortex-antivortex pairs, known as dipoles, the two dimensional equivalent of a smoke ring. As the dipoles carry linear momentum and energy, they obey a relation similar to Snell's law in optics. Preliminary data shows qualitative agreement between the trajectories of the dipoles and simulations. Overall these results demonstrate the versatility of the apparatus, for investigating vortex dynamics, suggesting several future areas of experimental interest.

Acknowledgements

I am exceptionally grateful to my supervisors Dr Tyler Neely and Dr Matthew Reeves. Without their help this thesis would not be possible. Tyler has been an amazing supervisor. I am always stuck by not only Tyler's patience and knowledge but, also his calm attitude despite how many experimental issues arise, including two magnetic coils breaking, three lasers dying, me misaligning the optical system so badly I accidentally created an atom laser, and the cooling system spraying water all over the optics table. Just as Tyler has been endlessly patient with the experiment, Matt has been equally patient and helpful with theory. Not only have I learnt a huge amount, but both Tyler and Matt have amazing role models and have deeply changed the way I think about physics.

Likewise I am thankful for Guillaume Gauthier who's enthusiasm is only matched by his infectious laughter. Guillaume has been a friend both inside the lab and out. Prof. Halina Rubinsztein-Dunlop has been hugely helpful arranging many of the logistical aspects of the project. I'm thankful for the guys in the lab; Maarten, Lauren, Alex, Tom, and Mark Baker, for both their companionship in the lab and friendship. I am also thankful to everyone who has previously worked on the experiment Nicholas Parry, Issac Lenton and Tom Carey. A huge thank you to our collaborators at the University of Otago, Xiaoquan Yu, Aston Bradley, and Michael Cawte. Special thanks is in order to all the EQUS and physics staff; Tara, Tara, Lisa, Murray, and a especially big thank you to Angie Bird.

I'd like to thank everyone in the physics honours cohort for getting through the year Ellie, Brad, Sam, and Aaron, Callum, Tim, and Ahmad in particular amongst many others. While not exactly physicists, this thesis would not be possible without Alex, Simran, Vaughan, Marc, Andrew, Tamati, Paul, Leah, Angel, James, Carrie and Joel for their friendship, goofiness, companionship, beta and belays.

Last and most importantly, I would like to thank the two people who have supported me the most. My parents Cliff and Mee Wun, for putting up with me for all these years. Without your love I couldn't have done it.

Contents

Abstract v

Acknowledgements vii

List of Figures xiii

List of Symbols and Acronyms xv

1 Introduction 1

1.1 The Project and Contributions 7

1.1.1 Chiral Clusters 8

1.1.2 Dipole Optics 8

2 Bose-Einstein Condensation 9

2.1 The Gross-Pitaevskii Equation 11

2.1.1 Healing length and Bogoliubov speed of sound 12

2.1.2 Quantum Fluids and Hydrodynamic formulation 12

2.1.3 Quantised Vortices as topological defects 13

2.2 The Point Vortex model 14

2.2.1 Circular Domain 17

2.2.2 Motion of vortices in inhomogeneous 2D Bose-Einstein condensates 18

3 **Onsager Clustering of point vortices** **19**

3.1 Onsager Vortex Clustering 19

3.1.1 Previous Experimental Observations of TWO SIGNED Onsager Clustering in BECs 21

3.1.2 Mean-Field theory of vortex clustering 23

3.1.3 Nonaxisymmetric clusters (Chiral System) 24

3.1.4 Motivation for experimentally exploring the chiral system 27

4 **Analogy to Snell's law** **29**

4.1 Reflection and Refraction of dipoles across a step-change in potential 29

4.2 On demand dipole generation using the "Chopsticks" method 32

4.2.1 Motivation for a Dipole optics experiment 33

5 **UQ experimental apparatus** **35**

5.1 Optical, Magnetic and Evaporative cooling 36

5.2 Optical control using the digital micromirror device (DMD 38

5.2.1 Half-toned optical potentials using the Floyd-Steinberg dithering algorithm 39

5.2.2 Feedforward method of creating desired potentials 41

5.3 Imaging 41

6 **Experimental observations of Onsager Clustering in the Chiral system** **45**

6.0.1 Vortex injection methods and 2D GPE simulations 46

6.0.2 Equivalence between GPE simulations and the point vortex model . . 50

6.1 Experimental results 52

6.2 Mapping experimental data onto Point Vortex Model 53

6.2.1 Imprinted vortices in a dynamic GPE simulation 54

6.2.2 Dynamic Point Vortex Model 56

6.3 Thermalisation and Demon Monte-Carlo 57

6.4 Symmetric breaking off-axis transition and parameter space 61

7 Dynamics of Vortex Dipoles and an analogy to Snell's Law 65

7.1 GPE simulations 66

7.2 Experimental dipole optics 67

7.2.1 Hard interface 69

7.2.2 Linearly varying density 69

8 Conclusion 75

8.1 Summary 75

8.2 Outlook 76

A Computational solving the GPE 79

References 83

List of Figures

1.1 Examples of large vortices in two dimensional fluids 2

1.2 Parameter space of the chiral system 4

1.3 Experimental images of a straight dipole trajectory in a homogeneous BEC . 6

2.1 Examples of vortex lattices in superfluids and superconductors 13

2.2 Trajectory of a dipole using the point vortex model 16

3.1 Negative temperatures as a consequence of bounded phase volume for a system of point vortices 20

3.2 Previous experimental observation of Onsager clusters at UQ 22

3.3 Parameter space of the chiral system 23

3.4 Negative temperature off-axis transition at high energies 26

4.1 Snell's law relation for vortex dipoles 31

4.2 Experimental demonstration of "chopsticks" dipole nucleation technique . . . 32

5.1 Experimental vacuum system, and major components 36

5.2 Science cell and 3DMOT 38

5.3 BEC flase coloured images 39

5.4 Digital micromirror device (DMD) 40

5.5 Faraday imaging 42

6.1 GPE simulation of the centre pinning vortex nucleation 48

6.2 GPE simulation of the single sweep vortex nucleation 49
6.3 GPE simulation of the double sweep vortex nucleation 50
6.4 Comparision of the GPE and Point vortex models 51
6.5 Vortex injection methods, experimental images, and vortex detection algorithm 52
6.6 Point Vortex data 54
6.7 Imprinted GPE vortex simulation in comparison to experimental data 55
6.8 Dynamic point vortex simulations using a diffusion term, compared to experimental data 56
6.9 Histograms of vortex clustering over time, compared to Monte-Carlo Histograms 58
6.10 Histograms of experimental nearest neighbour histograms of vortices 59
6.11 Demon Monte Carlo dipole momentum simulation 60
6.12 Time Integrated vortex histograms, compared to Monte-Carlo 61
6.13 Dipole moment transition above the critical energy 61
6.14 Parameter space from Monte-Carlo 62

7.1 Dipole Nucleation using the “chopsticks” technique 66
7.2 Example vortex trajectories simulated using the GPE 67
7.3 Reflection and refraction of dipoles across a step potential, simulated using the GPE 68
7.4 Experimental images of half-toned step potentials and chopsticks 69
7.5 GPE simulations of vortex trajectories in linearly varying condensate 70
7.6 Dipole trajectory with $\theta = 0°$ 71
7.7 Dipole Trajectory with $\theta = 90°$ 72
7.8 Prelimary experimental data compared to GPE simulations 73
7.9 Prelimary experimental data compared to GPE simulations 74

A.1 Vortex detection from the GPE 82

List of Symbols and Acronyms

The following list of symbols is neither exhaustive nor exclusive, but may be helpful.

$\Psi(\mathbf{r}, t)$ . . . . . . Many body wavefunction commonly referred to as simply the wavefunction

ξ . . . . The healing length

τ . . . . The healing time

The following acronyms are also used widely throughout this thesis

BEC - Bose Einstein condensate

DMD - Digital Micromirror Device

GPE - Gross Pitaevskii equation

QT - Quantum turbulence

MOT - Magneto-Optical Trap

MC - Monte-Carlo

DMC - Demon Monte-Carlo

JRS - Jones-Roberts soliton

TOF - Time of Flight

1

Introduction

Since the first Bose-Einstein condensate (BEC) was created in 1995 [4], a wide range of new experimental possibilities have opened. These have allowed physicists to explore many of the remarkable and strange properties of quantum mechanics, on a macroscopic scale. There are now around 250 experimental and theory groups investigating the area of cold atoms, BECs and degenerate fermi gases (DFG), on every continent except from Antarctica, and even in low earth orbit aboard the ISS, a remarkable multinational achievement. Optical and magnetic manipulation offers an extremely high degree of control over dilute atomic BECs, allowing experiments on superfluid dynamics and particularly experimental research in quantum turbulence. The UQ BEC apparatus is ideal for experiments in two dimensional superfluid dynamics, due to its high resolution and almost arbitrary dynamic potentials, created with a digital micromirror device (DMD). The first area of investigation in this thesis

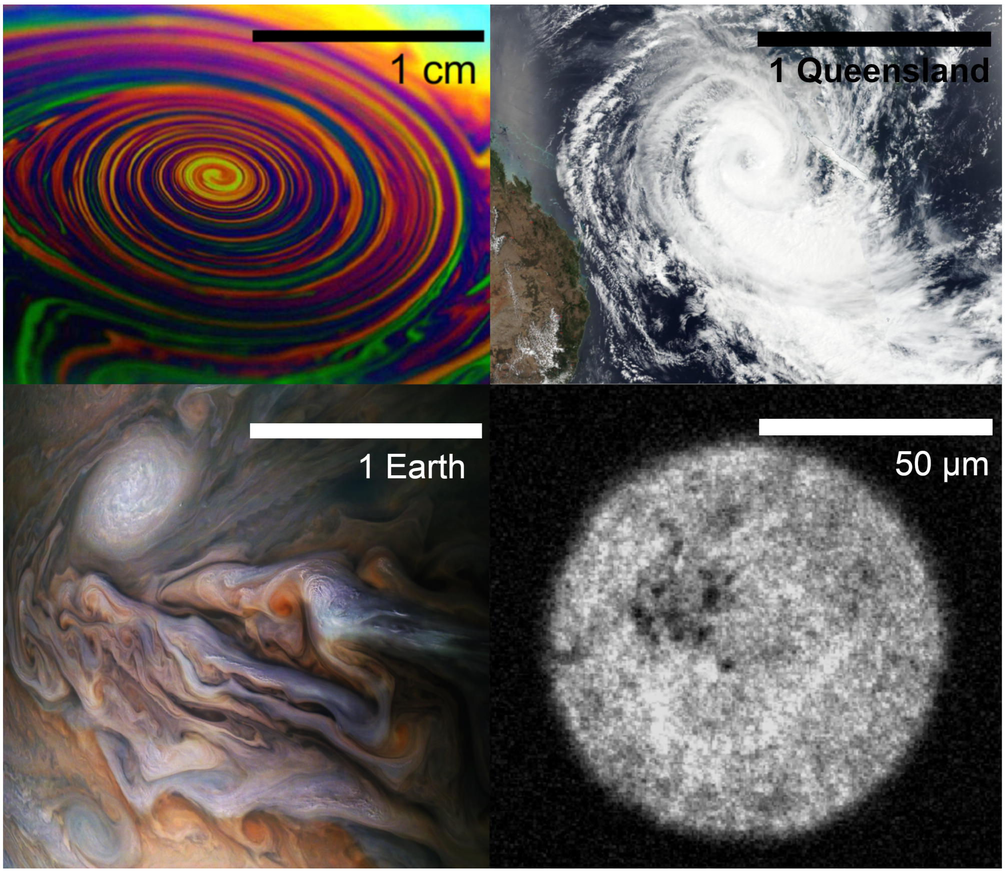

FIGURE 1.1: Examples of coherent structures across many length scales in two dimensional turbulence. Top left, a vortex in a soap bubble [1]; Top right, cyclone Oma [2]; Bottom left, jets and giant vortices in Jupiter's atmosphere [3]; and an Onsager cluster observed at the UQ BEC lab.

concerns quantum turbulence. While many aspects of quantum turbulence are well understood theoretically, there are presently many open questions that must be addressed with experiments. The first area of this thesis investigates a system of same-signed vortices, or the chiral system. We present the first observation of the long-predicted Onsager clustering in the chiral system, as well as observing non-axisymmetric vortex equilibrium states that are characterised at a negative absolute Boltzmann temperature. The second half of this thesis investigated the dynamics of a vortex-antivortex pairs, dipoles, and their motion in an inhomogeneous condensate. The dipoles can be shown to obey a Snell's law relation, as dipoles carry linear momentum and energy, and have curved trajectories, analogous to photons in a fibre optic cable.

Turbulence is one of the least understood areas of classical physics. This is because it occurs in continuous mediums with many, often infinite, degrees of freedom, leading to an interplay of order and disorder over many length scales. This leads to mathematical complexity which, despite hundreds of years of scientific inquiry, is still poorly understood. Despite some encouraging analytical results, such as Kolmorogov's celebrated energy spectrum [5], no theory has been able to describe how turbulence arises purely from the properties of the Navier-Stokes equations. Some of turbulences widely accepted upon properties include being: spatially and temporally irregular, non-local, non-Gaussian, non-integrable, and chaotic [6–11]. Simpler models of fluids, such as inviscid two dimensional fluids, are quite elucidating mathematically and yield a rich phenomenology [11, 12]. Two-dimensional turbulence features coherent rotational structures on scales ranging from soap bubbles, oceanic atmospheric phenomena on the planetary scale, and recently, at micrometer scales in BECs [13, 14]; displayed in Fig. 1.1. Somewhat unexpectedly quantum turbulence, turbulence arising from superfluids, is less mathematically complex than classical turbulence. Whilst an interesting area of research in its own right, it may provide insight into classical turbulence.

Perhaps the simplest model of a turbulent fluid is the point vortex model originally developed by Helmholtz [15] in 1858. Helmholtz showed that the vorticity of a single particle is conserved in two dimensions. By analogy to electrostatics or gravitating systems, the vorticity of the flow can be generated purely by N point sources (vortices) described by $2N$ coupled first order ODEs. This type of system displays rich mathematical behaviour which allows exploration of the transition to chaos, the deep connections between vortex equilibrium positions and roots of complex polynomials, applications of projective geometry, and the Weierstrass ζ function [16]. Physically, the point vortex model is an example of a system with long range interactions; other examples include astrophysical self gravitating systems, effective plasma models, spin systems and "toy models" [17, 18]. While the statistical mechanics of systems with long range interactions is still controversial, given that the partition function is no longer factorisable, these systems display rich and unexpected behaviour, such as having negative heat capacities in the micro-canonical formalism [17].

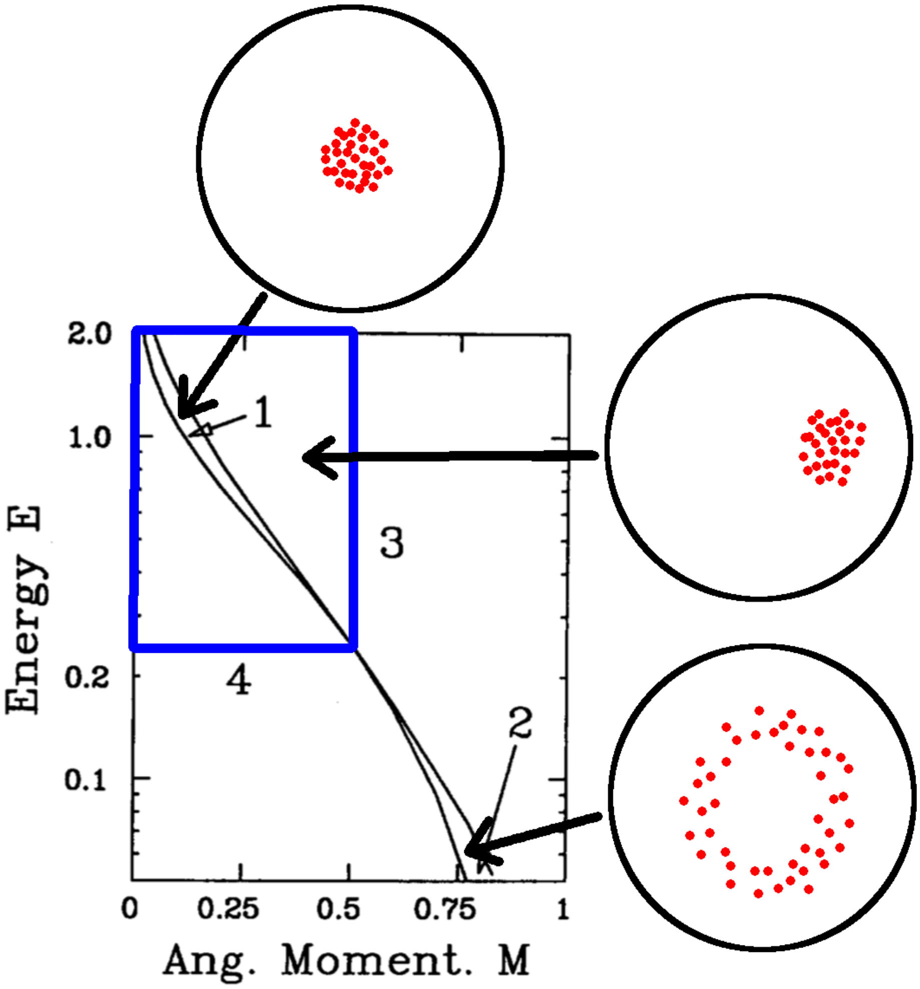

FIGURE 1.2: The parameter space of the same-signed vortex, chiral system, originally investigated by Smith and O'Neil [19]. The equilibrium configurations of vortices are completely characterised by the vortex energy and angular momentum. Region 1 on-axis vortex clusters equilibria. Region 2 vortex ring equilibria. Region 3 off-axis vortex cluster equilibria. Region 4 is a forbidden region due to constraints of the energy and angular momentum. The blue inset is the region of parameter space explored in this thesis. At high energies the equilibria transition from on-axis to off-axis due to competition between energy and angular momentum. This transition can only occur at a negative thermodynamic temperature.

Using the point vortex model, the scientific giant Lars Onsager, found a qualitative explanation for the large scale coherent flows found consistently in two dimensional fluids [12, 20] see FIG. 1.1. Similar statistical mechanical techniques have since been applied to model atmospheric phenomena [21], oceanic flows [22], Jupiter's Great Red Spot [23, 24] ,as well as the structure of stellar systems and galaxies [25, 26], amongst many others.

While vortices in a classical fluid can form and dissipate over time, vortices in a superfluid are quantised with circulation $\pm h/m$, where h is Planck's constant and m is the atomic mass. When in a sufficiently homogeneous condensate, these vortices exhibit an almost exact realisation of the point vortex model [12, 27, 28]. While Onsager's theory of clustering has been widely influential, only recent experiments with Bose-Einstein Condensates (BECs) have allowed realistic point vortex systems to be created. Onsager clustering of vortices in systems consisting of roughly even numbers of vortices and anti-vortices, has been recently observed by the UQ BEC lab [13], and by a group at Monash [14]. However, the chiral system has not been investigated experimentally, despite the system being well modelled with a variety of theoretical techniques by Smith and O'Neil in 1990 [19]. In this system, competition between vortex energy and angular momentum creates a transition between on-axis equilibrium vortex distributions at low energies, to off-axis equilibrium distributions at high energies, at a specified angular momentum. This resembles a second order phase transition, and can only occur at a negative thermodynamic temperature.

Experimentally, we have made the first observations of the chiral vortex clustering. Initial vortex states were deterministically created by sweeping optical blue-detuned paddles through the condensate, and modelled using the Gross-Pitaevskii equation, which gives a good description of the condensate for our experimental regime. The simulations were found to qualitatively agree with the experiment, giving us confidence that all the vortices are same-signed. We find excellent agreement between the vortex positions from the experiment and a dynamic point vortex model. We also find good agreement between the vortex positions a Monte-Carlo simulation, showing the vortices are in a thermal equilibrium. The second half of the present thesis investigates the trajectories of vortex-antivortex pairs (dipoles), in inhomogeneous condensates. In optics, Snell's Law is one of the most ubiquitous and useful equations. It was known to the Persian Scientist Ibn Sahl as early as 987 (some seven centuries before Newton's Philosophi Naturalis Principia Mathematica), before Willebrord Snellius (Snell) rediscovered it in 1621. Snell's law is a direct consequence of the conservation of linear momentum. Dipoles, in homogeneous condensates have linear trajectories and are

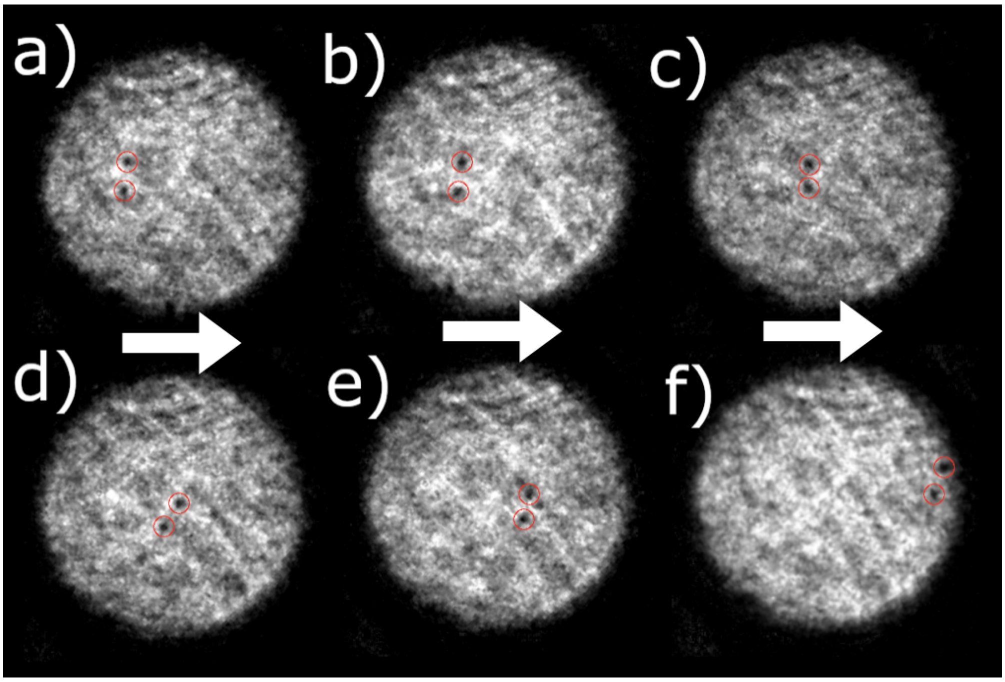

FIGURE 1.3: Experimental dipole, vortex-antivortex pair, positions in a homogenous condensate over time a)-f) with images taken every $25ms$. The dipole carries linear momentum and energy, suggesting an analogy to Snell's law.

the two dimensional equivalent of a smoke ring. As a dipole carries both linear momentum and energy we expect an analogous Snell's law to hold for a dipole passing through a step difference in condensate density. This has been shown to hold on both analytic grounds and with GPE simulations [29]. The experimental observation of dipole reflection or refraction across a step change in condensate density has proved challenging, even with the high degree of optical manipulation of the experiment provides. Instead we have opted to implement a linearly varying condensate density using a magnetic field. Dipoles travelling through the condensate now take curved paths, similar to sound waves in the atmosphere. The vortex separation, analogous to the frequency of a photon, can also be seen to change over the trajectory.

Regrettably, due to the large amount of subject matter, this thesis is very lengthy and has been divided into 8 chapters. Hopefully this keeps the content of each chapter somewhat self-contained and thematically consistent to the reader. The structure of remainder of this thesis is as follows. Chapter 2 covers a brief introduction to Bose-Einstein condensation, the

Gross-Pitaevskii equation, the hydrodynamic formulation, quantised vortices and the point vortex model. This forms the backbone of the theory content. This is quite well understood and many textbooks have been written on the subject including [27, 28, 30]. Chapter 3 covers Onsager's theory of vortex clustering in the point vortex model, the mean-field point vortex model, and the work of Smith and O'Neil [19], who investigate the chiral system. Chapter 4 covers the work of Cawte et al. [29], where the behaviour of a dipole is shown to obey a Snell's law relation. Also contained is a versatile experimental scheme for generating on demand vortex dipoles, with a high degree of control over initial vortex positioning. Chapter 5 covers the relevant aspects of the experiment that apply to Chapters 6 and 7, particularly the operation of the DMD, while much more thorough descriptions are presented in [31, 32] . Chapter 6 covers our experimental results of on-axis, off-axis and non-equilibrium initial vortex conditions in the chiral system with our analysis using the GPE, dynamic point vortex model, and Monte-Carlo methods. Chapter 7 covers GPE modelling of dipole trajectories across a step change and with an inhomogeneous change in condensate density. Preliminary experimental results dipole trajectories are also presented. Chapter 8 concludes with a summary and outlook.

Readers more interested in the theoretical basis of this thesis may find Chapter 5 less interesting and can skip details. Similarly readers less interested in theoretical background, may find Chapter 3 quite heavy and can pass onto the experimental results of the chiral system in Chapter 6, even though they share the same subject matter. Similarly Chapter 4 is followed by Chapter 7 thematically, choosing to read the chapters in this order may make the content flow better to the reader.

1.1 The Project and Contributions

This was a highly collaborative project. I first joined the UQ BEC lab for an undergraduate research project. I also did my capstone project with the same group, which originated the idea of the chiral clusters project. I elected to complete my honours degree over 3 semesters, with the honours thesis project over the last two. All of the experimental data, taken for the chiral cluster system, was performed in the first semester of my honours degree shortly prior to the commencement of the thesis project. As such it should not be considered as contributing to the thesis. However all of the numerical modelling of the chiral system has been completed during my honours project. BEC experiments are always collaborative due to the complex nature of the apparatus, and the nature of day to day operation.

1.1.1 Chiral Clusters

This experiment is closely related to the experiment that Guillaume performed [13], so much of numerical tools required to investigate this system, such as the vortex detection algorithm and dynamic point vortex model were readily available. Contributions as a rough percent for this experiment, and its numerical investigation are displayed below

Project	Kwan	Tyler	Matt	Guillaume
GPE Simulations	95	0	5	0
Dynamic PV simulations	20	0	80	0
PV Monte-Carlo	40	0	60	0
Experimental data	33	33	0	33

1.1.2 Dipole Optics

Rough contributions as percentages for the second project

Project	Kwan	Tyler	Matt	Guillaume
GPE Simulations	100	0	0	0
Experimental data	70	15	0	15

2

Bose-Einstein Condensation

Bose-Einstein condensates were first theorised by Albert Einstein in 1925, after correspondence with Satyendra Nath Bose. Bose investigated the statistics of photons, which are indistinguishable and symmetric under particle exchange, and have markedly different behaviour to classical particles. This represented a radical new understanding of particles and created the field of quantum statistics. More than 70 years after Einstein's initial prediction, atomic BECs were first created in 1995 by a research team lead by Eric Cornell and Carl Wieman, using ^{87}Rb atoms [4]. Their work was followed by a team led by Wolfgang Ketterle using ^{23}Na [33]. Cornell, Ketterle and Wieman were jointly awarded the 2001 Nobel prize for their contributions.

Atomic BECs, dilute vapours held in a vacuum, are easily manipulated with magnetic and optical fields. The weakly interacting individual atoms allow for a high degree of control over the atom's internal quantum states. This allows numerous methods of cooling, imaging and manipulating the condensate. Cold atom experiments have now been formed with 17 different elements as well as numerous isotopes, molecules and mixtures [28].

A qualitative understanding of Bose-Einstein condensation there is critical temperature T_C where the atomic thermal de Broglie wavelength, $\lambda_T = \sqrt{\frac{2\pi\hbar^2}{mkT}}$, is comparable to the inter-atomic distance. When this occurs, the atoms become spatially indistinguishable, and form a macroscopic coherent wavefunction. This occurs at a temperature on the order of

$$T_c = C\frac{\hbar^2 n^{2/3}}{mk}, \tag{2.1}$$

where C is a numerical factor. Bose-Einstein condensation can be considered more rigorously by looking at macroscopic occupation of the groundstate. The symmetry of bosons under particle exchange leads to "bosonic enhancement", where bosons have a preference for occupying the same state, compared to classical particles, and opposed to fermions which are anti-symmetric obey the Fermi-exclusion principle. Bosons are thermally excited into higher energy state preventing them from sharing the groundstate. However, at a sufficiently cold temperature, the bosonic enhancement overcomes the thermal fluctuations and the atoms "condense" into the groundstate analogous to condensation of water. In the case of non-interacting bosons, the occupancy of energy levels is given by the famous Bose-Einstein distribution

$$n_i(\varepsilon_i) = \frac{g_i}{e^{(\varepsilon_i-\mu)/kT} - 1}, \tag{2.2}$$

where g_i is the degeneracy, μ is the chemical potential, ε_i is the energy level of the *ith* particle, k is Boltzmann's constant, and T is the temperature. Einstein showed there is a certain critical temperature, T_C, at which a macroscopic occupation of the groundstate is achieved. In the case of no interactions allowed energy states are given by the Schroedinger equation, and in the many particle limit, the particle density is well approximated by $n(\mathbf{r}) = |\Psi(\mathbf{r})|^2$, where $n(\mathbf{r})$ is the number density of particles in the groundstate, rather than the number occupancy of an energy level given by Eqn. 2.2.

2.1 The Gross-Pitaevskii Equation

The Gross-Pitaevskii equation (GPE) was independently developed by Eugene Gross [34] and Lev Pitaevskii [35] around 1961, both in an effort to investigate the structure of quantised vortices. The Gross-Pitaevskii equation describes a many-body wavefunction, rather than the single body wavefunction in the Schroedinger equation. The GPE describes the BEC as a semi-classical field, as in the many particle limit, $N >> 1$, we can approximate $a^\dagger a = aa^\dagger = N$, where we have neglected the commutator $[a, a^\dagger] = 1$ as the addition of an additional particle will have little effect on particle number or chemical potential. Deriving the GPE uses a mean-field approximation and considers only two body s-wave scattering collisions. It accurately models the dynamics of a single species weakly interacting dilute gas BEC at zero temperature.

$$i\hbar\frac{\partial}{\partial t}\Psi(\mathbf{r},t) = \left(-\frac{\hbar^2\nabla^2}{2m} + V_{ext}(\mathbf{r},t) + g|\Psi(\mathbf{r},t)|^2\right)\Psi(\mathbf{r},t), \tag{2.3}$$

where $g = 4\pi\hbar^2 a/m$, a is the s-wave scattering length, V_{ext} is an externally applied potential, and m is the mass of the bosons. For ^{87}Rb, the interaction between atoms are repulsive, so $g > 0$.

Under certain conditions the kinetic energy term becomes negligible compared to the potential and interaction terms. Neglecting the kinetic energy term is known as the Thomas-Fermi approximation, and provides a simple expression for the density,

$$n(\mathbf{r}) = |\Psi(\mathbf{r})|^2 = \frac{\mu - V_{ext}(\mathbf{r})}{g}, \tag{2.4}$$

where μ is the chemical potential and $\mu = gn$ for a homogenous condensate. The chemical potential is given by $\mu = \frac{\partial E}{\partial N}$. The Thomas-Fermi approximation can be interpreted as a solution requiring the same amount of energy to add an extra particle anywhere in the condensate. This is a good approximation of the groundstate in our experiment which typically has several million atoms [27, 28]. By changing the applied potential, we can manipulate condensate groundstate.

2.1.1 Healing length and Bogoliubov speed of sound

It is very useful to define a coherence length of the condensate, a distance comparable of that where a homogeneous condensate regains its bulk value close to local perturbation. By assuming the boundary conditions $\psi(0) = 0$ and $\psi(\infty) = \psi_0$ and no external potential, we obtain the analytic solution

$$\psi(x) = \psi_0 \tanh\left(\frac{x}{\xi}\right), \tag{2.5}$$

where the healing length is defined as $\xi^2 = \hbar^2/mng$. An excitation will travel at the Bogoliubov speed of sound $s = \sqrt{ng/m} = \hbar/m\xi$. This allows us to define a natural time unit known as the healing time $\tau = \xi/s = m\xi^2/\hbar$.

2.1.2 Quantum Fluids and Hydrodynamic formulation

From the Gross-Pitaevskii equation, we can directly derive the hydrodynamic equations. We re-express the wavefunction in terms of the density and phase $\Psi = \sqrt{n}e^{i\phi}$, with the phase defined as $\phi(\mathbf{x}, t) = \arg(\Psi)$. The velocity field given by

$$\mathbf{v}(\mathbf{r}) = \frac{\hbar}{m}\nabla\phi(\mathbf{r}). \tag{2.6}$$

It is then possible to derive the Hydrodynamic equations

$$\frac{\partial \mathbf{v}}{\partial t} = -\frac{1}{mn}\nabla p - \nabla\left(\frac{v^2}{2}\right) + \frac{1}{m}\nabla\left(\frac{\hbar^2}{2m\sqrt{n}}\nabla^2\sqrt{n}\right) - \frac{1}{m}\nabla V \tag{2.7}$$

where m is the boson mass, n is the density, V is an applied potential, and $p = \frac{\partial E}{\partial V}$ is the pressure. This equation is analogous to the Euler equation from classical fluid dynamics that describes inviscid fluid flow

$$\frac{\partial \mathbf{v}}{\partial t} = \mathbf{v} \times (\nabla \times \mathbf{v}) - \nabla\left(\frac{v^2}{2}\right) - \frac{1}{mn}\nabla p - \frac{1}{m}\nabla V. \tag{2.8}$$

It is important to note that since $\nabla \times \mathbf{v} = 0$, unless a vortex is present, this term usually doesn't contribute. We also have the quantum pressure term $\frac{1}{m}\nabla\left(\frac{\hbar^2}{2m\sqrt{n}}\nabla^2\sqrt{n}\right)$ due to spatial variations in the magnitude of the wavefunction which has effects on scales smaller than the healing length [28]. This shows that a dilute weakly interacting bose gas obeys the same equations as a perfect inviscid fluid.

2.1.3 Quantised Vortices as topological defects

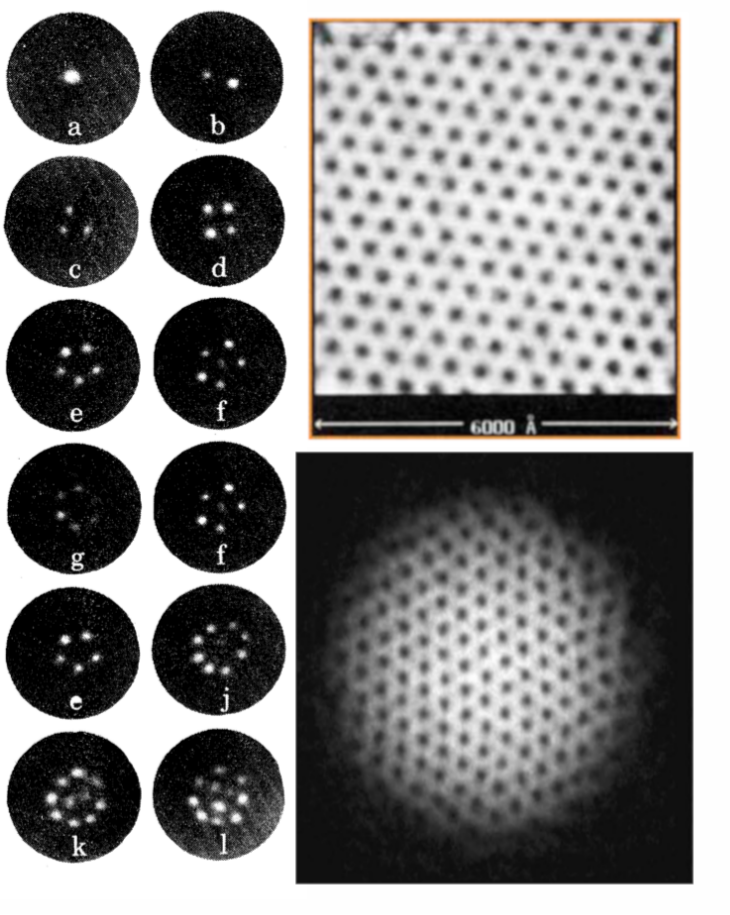

FIGURE 2.1: Quantised vortices in vortex lattices. These rigid body triangular lattices are the lowest energy states in a rotating superfluid. The images are from liquid ^{4}He, left [36], in a lattice of supercurrent flow, top right [37], and previously in BECs bottom right [38].

The vector-calculus identity, $\nabla \times (\nabla U) = 0$, where U is an arbitrary continuous scalar function, implies the velocity field given by equation 2.6 is irrotational, so long as θ is continuous. However, if there is a discontinuity in phase, the identity no longer applies and fluid rotation is permitted. Using the Cauchy residue theorem, integrating the phase around a closed path gives

$$\Delta\phi = \oint \nabla\phi \cdot \mathrm{d}\ell = 2\pi n, \quad \text{where } n \text{ is an integer,} \tag{2.9}$$

with the circulation given by

$$\Gamma = \oint \mathbf{v} \cdot \mathrm{d}\ell = \frac{\hbar}{m} 2\pi n = \frac{h}{m} n = \kappa n. \tag{2.10}$$

This means, unlike a classical fluid, vortices in a BEC are quantised in units of h/m[1]. The phase, θ, is continuous everywhere except for the vortex singularity, so the velocity of the superfluid grows to infinity approaching a vortex core. To avoid an infinite energies, the wavefunction density must go to zero towards the singularity. In three dimensions, this results in quantised vortex lines, and in two dimensions, it implies quantised point vortices (with some structure) [28]. These have been widely observed in superfluids and in superconductors. A striking example of this are triangular vortex lattices shown in Fig. 2.1. Due to the nature of the discontinuity in phase, single vortices cannot be created or destroyed in the middle of the condensate. Instead they can only be generated or annihilated in vortex-antivortex pairs, and single vortices can only introduced or leave the condensate through a boundary. It is also energetically favourable for two vortices to form rather than a single vortex of circulation $2h/m$, so any vortex in the condensate will have circulation $\pm h/m$.

2.2 The Point Vortex model

While the GPE is very accurate and takes into account density changes, surface waves, and other effects, the GPE is computationally expensive compared to the point vortex model. The point vortex equation can be derived from the Euler equation (equation 2.8) describes the dynamics of inviscid fluids. The vorticity field is defined in terms of the velocity as

$$\boldsymbol{\omega}(x, y, z) = \nabla \times \mathbf{v}(x, y, z). \tag{2.11}$$

The Euler equation in two dimensions can be expressed in terms of the vorticity as

$$\frac{D\boldsymbol{\omega}}{Dt} = 0, \tag{2.12}$$

where $D/Dt = \partial/\partial t + \mathbf{u} \cdot \nabla$. This is a conservation law stating vorticity can be transported, but not created or destroyed. Taking the limiting case where the circulation is generated by point sources, analogous to the use of point masses in celestial mechanics or point charges in electrostatics

---

[1] Interestingly this was present without proof as a footnote in Lars Onsager's 1949 paper on Hydrodynamic turbulence [12], then re-discovered by Feynman [39]

$$\boldsymbol{\omega} = \sum_{i}^{N} \frac{\Gamma_i}{2\pi} \delta^{(2)} \left(\mathbf{x} - \mathbf{x_i} \right), \tag{2.13}$$

where Γ_i is the circulation of the *ith* vortex. The velocity of the fluid is given by

$$\dot{\mathbf{x}} = \sum_{i}^{N} \frac{\Gamma_i}{2\pi} \cdot \frac{\mathbf{n}_i \times (\mathbf{x} - \mathbf{x}_i)}{|\mathbf{x} - \mathbf{x}_i|^2}, \tag{2.14}$$

where $\mathbf{n_i}$ is the normal vector to the fluid and the point vortex equations of motion are

$$\dot{\mathbf{x_j}} = \sum_{i}^{N} \frac{\Gamma_i}{2\pi} \cdot \frac{\mathbf{n}_i \times (\mathbf{x_j} - \mathbf{x}_i)}{|\mathbf{x_j} - \mathbf{x}_i|^2}. \tag{2.15}$$

The Hamiltonian formulation is then given by

$$H = -\frac{1}{4\pi} \sum_{i \neq j} \kappa_i \kappa_j \log r_{ij}, \tag{2.16}$$

where κ_i is the circulation of the *ith* vortex, and r_{ij} is the distance between the *ith* and *jth* vortices, and Hamilton equations of motion by

$$\kappa_i \frac{\mathrm{d}x_i}{\mathrm{d}t} = \frac{\partial H}{\partial y_i}, \tag{2.17}$$

$$\kappa_i \frac{\mathrm{d}y_i}{\mathrm{d}t} = -\frac{\partial H}{\partial x_i}. \tag{2.18}$$

For this system x_i and y_i are canonically conjugate variables, as opposed to the typical canonical variables x and $p = m\frac{\partial x}{\partial t}$ a more typical system. This results in a first order ODEs describing the point vortex dynamics. The fact that x_i and y_i are the canonically conjugate variables has profound implications for phase space as we'll see in Chapter 3.

Image vortices

In a bounded system, the fluid velocity across a boundary is zero. This can be accomplished by the use of Green's functions whereby an "image vortex" is placed to cancel the fluid across the boundary mathematically equivalent to the use of image charges in electrostatics. The Hamiltonian formulation is a conservative system, so vortices that stray close to the boundary pair up with their image vortices and travel around the boundary until they pair

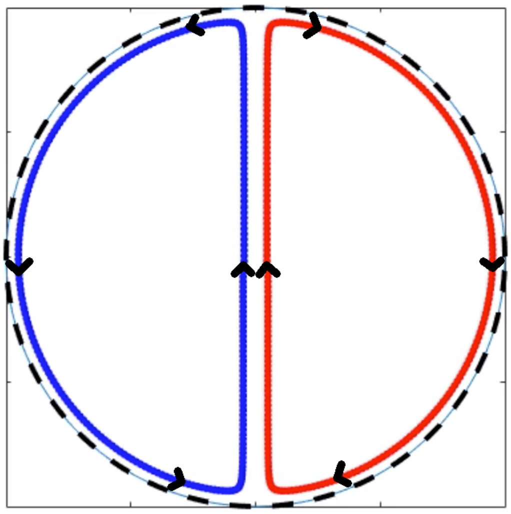

FIGURE 2.2: Trajectory of a dipole, vortex-antivortexp pair, computed using the point vortex model. The dipole carries linear momentum and travels in a straight line until the vortices pair up with their images close to the boundary. Here the vortices travel around the boundary, constrained by the image charges, until they pair up again and form a closed orbit.

up with another vortex. In a circular domain a vortex dipole will move in a straight line until the vortices pair up with their images. These vortices will then travel around the boundary of the condensate until they pair up with their original vortices forming a dipole again and completing a closed orbit, see Fig. 2.2 for the dipoles trajectory. The use of image vortices is extremely important both for understanding and modelling the system.

Noether's theorem and conserved quantities

Noether's theorem, put roughly, states that corresponding to every continuous transformation which leaves the Lagrangian invariant, there exists a conserved quantity. For a system of point vortices, we have

- Invariance under time → energy conservation
- Invariance under spatial translations → conservation of linear momentum
- Invariance under rotations → conservation of angular momentum

All of these quantities are conserved for a boundless system. The point vortex system has $2N$ degrees of freedom. More details on the derivation of the point vortex model can be found in the N-Vortex problem [30]. It needs to be stressed that the vortex energy and angular momentum are separate quantities to the condensate energy and angular momentum; however, they are closely related. It is also possible, and very useful, to reformulate these equations using complex numbers, where express $z = x + iy$. This effectively reduces the number of equations by two and the form of the equations are simplified.

2.2.1 Circular Domain

The simplest bounded system is the circular disk, it was the trapping potential implemented in both experiments. For circular domain, corresponding to every vortex is an image vortex at $\bar{r}_k = \frac{r_k R^2}{|r_k|^2}$, where R is the trap radius. The Hamiltonian for this system is

$$H = -\frac{1}{4\pi}\sum_{i\neq j}\Gamma_i\Gamma_j \ln\left|\frac{\mathbf{r}_i - \mathbf{r}_j}{R}\right| - \frac{1}{4\pi}\sum_{i,k}\Gamma_i\Gamma_j \ln\left|\frac{\mathbf{r}_i - \bar{\mathbf{r}}_k}{R}\right|, \tag{2.19}$$

and the angular momentum

$$M = \frac{1}{2}\sum_{j=1}^{N}\Gamma_j r_j^2. \tag{2.20}$$

For the circular domain these are the only integrals of motion. The time evolution of more than two vortices is expected to be chaotic in contrast to the unbounded domain case which has three integrals of motion [40]. While not a conserved quantity, an extremely important characterising parameter is the dipole moment

$$D = \sum_i s_i x_i \hat{\imath} + \sum_i s_i y_i \hat{\imath},$$

where $s_i = \pm 1$ is the sign of the vortex. This is a vector quantity, however we also refer to its magnitude as the dipole moment. The dipole moment is a measure of the symmetry of a system. For a system of same signed vortices, the dipole moment is the average position of the vortices.

2.2.2 Motion of vortices in inhomogeneous 2D Bose-Einstein condensates

Alternatively the point vortex model can be derived from the GPE. It is possible to extend the point vortex model, equations 2.16, 2.17, and 2.18, to non-homogeneous fluids by adding a density gradient term. Groszek et al. [41] found equations of motion for point vortices in a non-homogeneous condensate. Typically, in the literature, a phenomenological term is added to the point vortex model to account for the motion of vortices close to the centre of a harmonic trap. Groszek et al. derive a point vortex equation which has previously been found in the literature [42–44] but not utilised. They show that this point vortex model agrees excellently with the Gross-Pitaevskii equation in a harmonic potential [41].

If we assume evolution of the system is given by a non-linear Schroedinger equation of the form $i\hbar\partial_t\Psi = \mathcal{H}\Psi$ with the Hamiltonian

$$\mathcal{H} = -\frac{\hbar^2}{2m}\nabla^2 + \mathcal{U}(\mathbf{r}, t). \tag{2.21}$$

A singly charged quantised vortex at location $\mathbf{r}_\circ = (x_\circ, y_\circ)$, which can be expressed as $z_\circ = x_\circ + iy_\circ$ will have the local wavefunction

$$\Psi_\circ = (z - z_\circ)\tilde{\rho}e^{i\tilde{\phi}}, \tag{2.22}$$

where $\tilde{\rho}$ and $\tilde{\phi}$ are smoothly varying functions which represent the density and phase in the absence of a vortex. The velocity of the vortex is then given by

$$\begin{aligned} \mathbf{v_v}(\mathbf{r}_\circ) &= \frac{\hbar}{m}\left(\nabla\tilde{\phi} - \hat{\kappa} \times \nabla \ln \tilde{\rho}\right)|_{\mathbf{r}_\circ} && (2.23) \\ &\equiv \mathbf{v_s}(\mathbf{r}_\circ) + \mathbf{v_d}(\mathbf{r}_\circ), && (2.24) \end{aligned}$$

where we have a superfluid velocity $\mathbf{v_v}$ due to ambient phase gradients $\mathbf{v_s}(\mathbf{r}_\circ) = \hbar/m\left(\nabla\tilde{\phi}\right)$ and a density gradient velocity $\mathbf{v_d}(\mathbf{r}_\circ) = -\hbar/m\,(\hat{\boldsymbol{\kappa}} \times \nabla \ln \tilde{\rho})$. This formulation of the point vortex model was shown to agree very well with simulations of the GPE in a harmonic potential.

3

Onsager Clustering of point vortices

3.1 Onsager Vortex Clustering

In his influential 1949 paper “Statistical Hydrodynamics”, Lars Onsager explores the statistical mechanics of a system of point vortices. Onsager considers a system of point vortices, with the Hamilton equations of motion, Eqn. 2.17 and 2.18. For homogeneous with with an arbitrary domain the Hamiltonian will be of the form

$$H = -\frac{1}{4\pi}\sum_{i\neq j}\kappa_i\kappa_j \log r_{ij} + \text{(image vortex potential)}, \tag{3.1}$$

where r_{ij} is the distance between vortices, and image vortices dependent on the confining geometry. If the fluid is confined to a finite area A, some unusual properties emerge. In the point vortex model, the canonical conjugates are x and y and the phase space is equal to the configuration space $\mathrm{d}\Omega = \mathrm{d}x_1\,\mathrm{d}y_1\cdots\mathrm{d}x_n\,\mathrm{d}y_n$. The total area of the phase space is given by

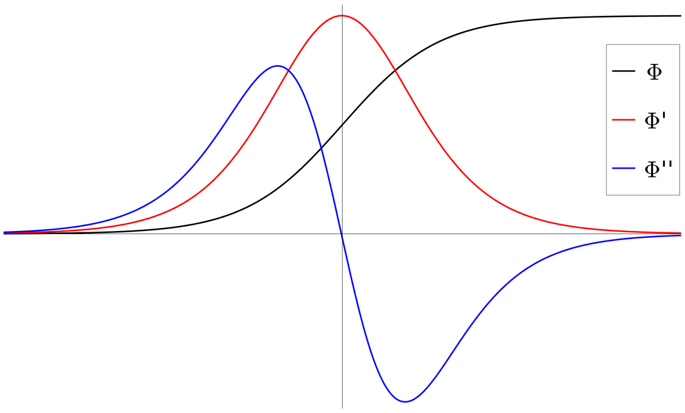

FIGURE 3.1: The temperature of a point vortex system can be defined as $\Theta = \Phi''/\Phi'$, where $\Phi(E) = \int_{H<E} \mathrm{d}\Omega$ is the phase volume. This is the volume of phase space with energies below E [12, 30]. Since $\Phi(E)$ is monotonically increasing from 0 to the total area of phase space A^n, it is a bounded function and must have asymptotes as $E \to \pm\infty$. A bounded monotonically increasing function must also have a point of inflection. As Φ is monotonically increasing, the derivative of the phase volume $\Phi'(E)$ must always be positive. The second order derivative Φ'' must also switch from being strictly positive when $E < E_m$, to zero at $\Phi''(E_m) = 0$, to negative as $E > E_m$. This that for $E < E_m$ the temperature is positive. For high energies above the critical energy, $E > E_m$, the temperature must be negative.

the integral over the phase space $\int \mathrm{d}\Omega = (\int \mathrm{d}x\, \mathrm{d}y)^n = A^n$. Onsager defines the phase-volume as the volume of phase-space below a certain cut-off energy $H(x_1, y_1, \cdots x_n, y_n) < E$

$$\Phi(E) \equiv \int_{H<E} \mathrm{d}\Omega \tag{3.2}$$

$$= \int_{-\infty}^{E} \Phi'(E)\, \mathrm{d}E\,. \tag{3.3}$$

This has the limiting cases of $\Phi(-\infty) = 0$, where two opposite signed vortices are on top of each other, and $\Phi(\infty) = A^n$, which is the total area of the phase space. We also have that $\Phi'(E) > 0$ for all E, and has a maximum value at some energy with $\Phi''(E_m) = 0$. For energies below E_m, the temperature is given by $\Theta = \Phi''/\Phi'$ with $\infty > 1/\Theta > 0$, while at higher energies $E > E_m$ we have $0 < 1/\Theta < -\infty$. This definition of temperature is equivalent to defining the entropy as $S = \ln \Phi'(E)$. This negative temperature behaviour is illustrated in Fig. 3.1.

Based purely on constraints of the phase-volume, we see that vortices must have a negative thermodynamic temperature at high energies. This implies that opposite signed vortices will cluster together in dipoles at positive temperature (low energies) while at negative temperatures (high energies), same signed vortices will cluster. While the vortices want to spread share the energy between them, the constraint of high energy causes like-signed vortices to cluster together, see Fig. 3.2 to see the like-signed clustering, and opposite-signed clustering in a real system. Any weaker or other signed vortices will have a negligible contribution to the larger flow. Prediction is a remarkable result based only on the assumption that the vortices are confined in a finitely domain.

Onsager remarks that the point vortex model doesn't apply to most normal fluids in which the flow is continuous and that vorticity emerges from bringing together same signed vortices. The creation and destruction of vorticity is beyond this model. However Onsager predicts that the vortices in a superfluid are quantised with circulation h/m, so superfluids are a candidate for the point vortex model[1].

3.1.1 Previous Experimental Observations of TWO SIGNED Onsager Clustering in BECs

Onsager clustering has been directly observed in BECs only recently. Observation of a neutral vortex system, a system with equal numbers of vortices and anti-vortices, at the University of Queensland was performed by sweeping optical paddles through the condensate to nucleate two opposite signed vortex clusters, which mean-field theory predicts is close to an equilibrium state. The vortex clusters in such a system are in equilibrium and long lived. This was compared to a more spatially random distribution of vortices created by a sweep of barriers through the condensate, which do not appear to cluster [13].

At Monash University, Johnstone et al. [14] have observed vortex structures emerging out of a random distribution of vortices. These were created by a sweep of barriers through the

---

[1] Much of Onsager's work on hydrodynamic turbulence remained unpublished as private notes and correspondences and and of Onsager's results were subsequently rediscovered years later [20].

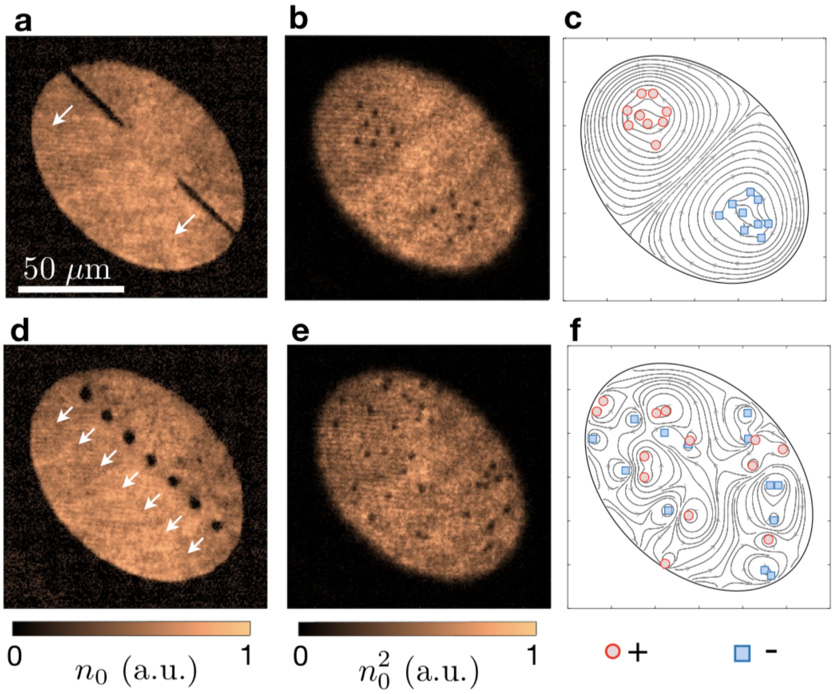

FIGURE 3.2: From [13] Onsager clustering in the neutral system a) Sweeping optical paddles through the condensate in order to create vortex clusters, b) vortex clusters shortly after nucleation, clearly clustering in like-signed vortex distributions, a high energy state, c) visualisation of the flow field from the point vortex model. d) creation of random signed vortices using a barrier sweep, e) random distribution of vortices, with opposite-signed vortex clustering, a low energy state, f) the spatially disordered flow field.

condensate. The vortices form larger flows through a process called evaporative heating, whereby energy is lost from the least energetic vortices as they pair up into dipoles and annihilate. Using Bragg imaging, which splits the condensate into the velocity field of the condensate towards and away from the Bragg beam, the velocity field of the vortices can be reconstructed. This can be used to detect the sign of individual vortices by comparison of the flow field generated by point vortices. These point vortices can then be classified by an algorithm which looks at number of free vortices, vortex pairs and vortex clusters. This is compared to simulations and assigned a temperature based on the clustering statistics.

These results have been interesting, however the behaviour of the two-signed vortex system quite different as we'll see in Section 3.1.3. The previous study by Gauthier [13] simply investigated the stability of initially injected vortex and anti-vortex clusters and compared the clustering statistics to a random initial distribution of vortices, with no investigation of the relaxation into the equilibrium state. The study by [14], doesn't inject vortices deterministically, so the energies and angular momenta of an initial configuration are not controlled. While vortex clustering was observed, due to the evaporative heating mechanism the vortex number changes rapidly making it hard to explore the parameter space.

3.1.2 Mean-Field theory of vortex clustering

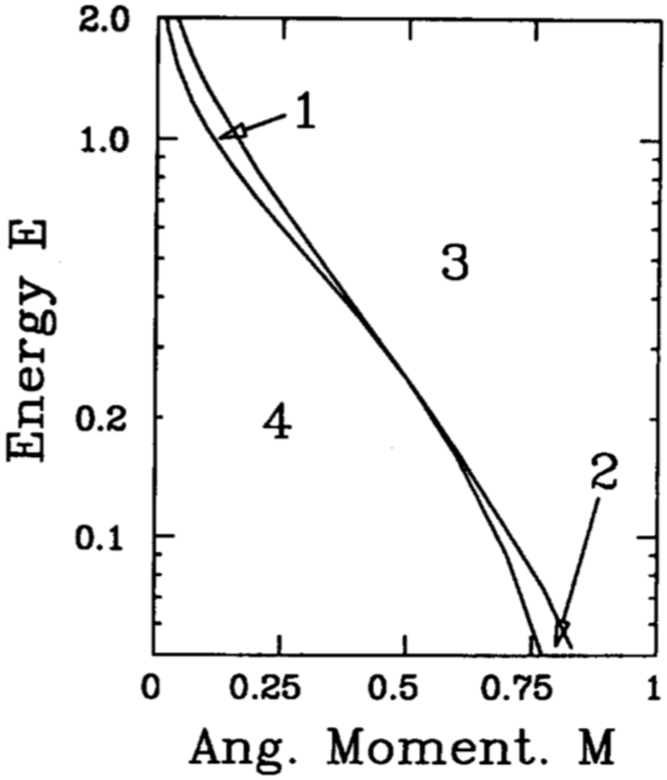

FIGURE 3.3: Parameter space of Onsager vortex system. Region 1 corresponds to on-axis vortices distributed around the centre. Region 2 corresponds to on-axis vortices distributed around the edge. Region 3 corresponds to Onsager vortices off-axis. Region 4 is prohibited as there are no states which can posses the required angular momenta and energies. Figure taken from Smith and O'Neil 1990 [19].

Joyce and Montgomery (1973) first developed a mean-field theory to describe equilibrium distributions of the guided centre plasma model, equivalent to equilibrium vortex cluster positions [45]. They derive this by computing phase space volumes in the large N limit. The mean-field description is given by the Poisson-Boltzmann equation

$$\nabla^2\psi = \exp\left(\mp\beta\psi \mp \omega r^2\right) \tag{3.4}$$

where ψ is the stream potential, β is the thermodynamic temperature, ω is a Lagrange multiplier corresponding to the rotation frequency, and $\nabla^2\psi = -4\pi n(\mathbf{r})$. The neutral system, with equal positive and negative vortices, has attracted much interest and can be re-expressed as a sinh equation. Numerical solutions have been explored in [46, 47] with direct comparisons to GPE and point-vortex simulations also performed in [48, 49], for solutions on a disk and in a box respectively. GPE and point vortex simulations have been found to be in good agreement with mean field theory. The mean-field model predicts self-organisation of vorticity into large scale flows on the scale of the domain. The theory of the single-singed system in a circular trap has been explored in detail by Smith and O'Neil in their 1990 paper "Non-axisymmetric thermal equilibria of a cylindrically bounded guiding-centre plasma or discrete vortex system" [19].

3.1.3 Nonaxisymmetric clusters (Chiral System)

For a system of same-signed vortices, dominant configurations at high energies shift off-axis, for a fixed value of angular momentum. This transition breaks the symmetry of the system and occurs due to competition between angular momentum, $M = \sum_i r_i^2$, which keeps the vortices at a certain distance away from the centre of the trap, and the energy, which causes the vortices to cluster. The transition between the on-axis and off-axis clusters resembles a second order phase transition and occurs at negative temperatures. Smith and O'Neil investigate this behaviour by using a mean-field approach and comparing it to Monte Carlo simulations [19][2].

---

[2] For consistency with the rest of this thesis, I will refer to this system as the chiral system as it is no-longer mirror symmetric, due to the symmetry breaking transition. I will also refer to the equilibrium axisymmetric states as on-axis clusters (unless they are ring states), and the non-axisymmetric states as off-axis clusters, unlike Smith and O'Neil.

The mean-field equation for the chiral system can also be expressed as

$$n(r) = n_0 \exp\big(4\pi\beta\nabla^{-2}n - \omega\beta r^2\big), \tag{3.5}$$

Where $\nabla^{-2}n$ is shorthand for the solution to the Poisson equation with $\phi = 0$ at $r = 1$, and subject to the constraints

$$\int n\,\mathrm{d}A = 1, \quad E = \frac{1}{2}\int n\phi\,\mathrm{d}A\,, \quad M = \int r^2 n\,\mathrm{d}A\,. \tag{3.6}$$

Smith and O'Neil (1990) note that Eqn. (3.5) is the approximate solution of the micro-cannonical ensemble in the large N limit and can be derived in a number of different ways which all assume that certain correlations are all weak [50**?** **?** –52]. The finite boundary and constraints on the angular momentum lead to thermal equilibria with a non-trivial mean field. By fixing the angular momentum it is possible to find the explicit dependence of the entropy (S) and inverse temperature (β) on the energy (E).

The entropy is maximised if the vortices form a single cluster single cluster. Smith and O'Neil also note that a simple picture of understanding the off-axis transition comes from the Boltzmann distribution Eqn. (3.5). In this equation, β can be seen to change the interaction between the vortices from repulsive at positive temperature to attractive at negative temperature. The ωr^2 term represents the rotation of the cluster and can be considered as a centred repulsive hill potential, equivalent to a centrifugal force. At low energies and low angular momenta, the interaction between the vortices and their image charges will form an effective potential in the centre of the condensate causing the vortices to cluster on-axis, with no centred repulsive hill to repulse vortices. At low energies and high rotation, the vortices will be repulsed by this central potential and form a ring state. At high energies, the centre of the repulsive potential and the image potential is at some distance, $0 < D < R$, where D is the dipole moment, which the vortices will cluster around due to the vortices self-attraction. They note that the mean-field model indicates that the symmetry is broken continuously indicating a resemblance to a second order phase transition. The dipole moment changes continuously with large fluctuations near the transition energy, and is given approximately by $\langle D\rangle = \sqrt{E - E_c}$, above this critical energy.

By linearising the mean-field equations they explore the behaviour of the vortex distribution, at a fixed angular momentum, by varying the energy. At energies greater than the transition energy ($E > E_c$) there is a bifurcation, with an on-axis and off-axis solutions, to the mean-field equation. The off-axis solution is the thermodynamically stable configuration which maximises the entropy.

Monte-Carlo simulations

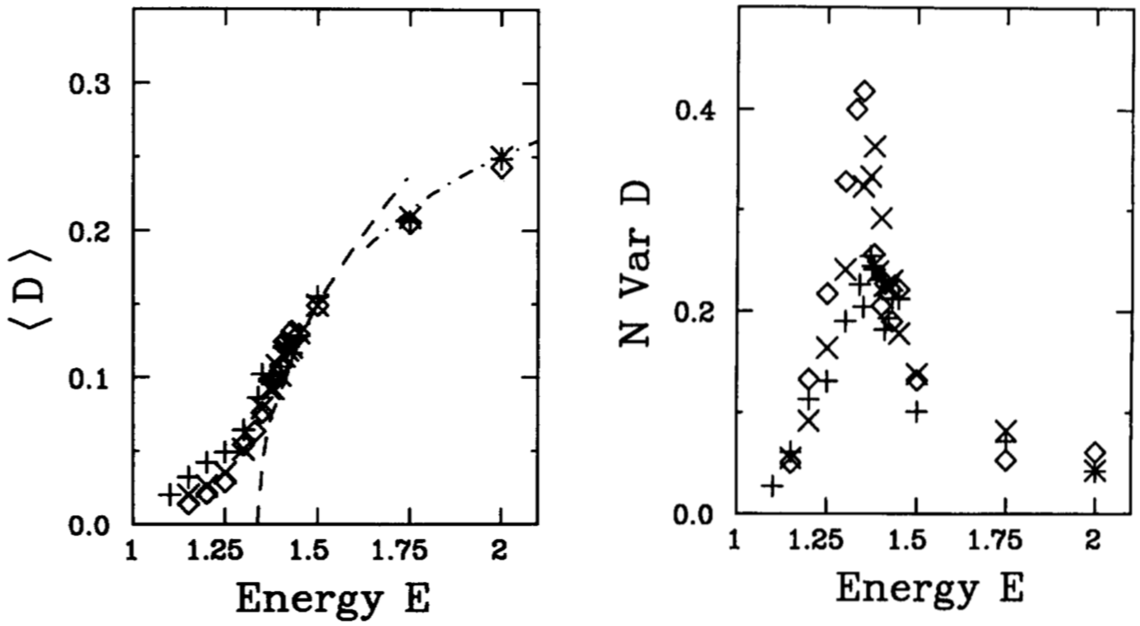

FIGURE 3.4: The lines are the result of numerically solving the mean-field equations. The solid line represents the symmetric branch, the dashed line represents perturbative bifurcation theory, and the dashed dotted line represents the high energy approximation. The symbols are the result of the demon Monte-Carlo simulations. With vortex numbers of +, N = 256; ×, N = 512; ⋄, N = 1024. Figure taken from [19]

Smith and O'Neil then explore the system using a modified version of Creutz's micro-canonical Monte-Carlo algorithm, known as a demon Monte Carlo technique. The demon is an extra degree of freedom that has some small energy and angular momentum range $|E_d| < E_M$, $|M_D| < M_M$. Two random particles are chosen and perturbed into a new configuration, which is only accepted if the change to the energy and angular momentum is within the tolerances of the demon. The total energy and angular momentum are then given by

$$E_T = E_D - \sum_{i \neq j} \log |\mathbf{r}_i - \mathbf{r}_j| + \sum_{i,j} \log\bigl(\mathbf{r}_j |\mathbf{r}_i - \mathbf{r}_j| / r_j^2\bigr) \tag{3.7}$$

$$M_T = M_D + \sum_j r_j \tag{3.8}$$

The demon can be thought of as being in thermal contact with a heat reservoir and has a Maxwell distributions which can be used to find the temperature of the ensemble.

As mentioned in Section 2.2.1, the dipole moment is an important charactering parameter, and for the chiral system, is equivalent to the average vortex position. For a given angular momentum the dipole moment will be zero up until a critical transition energy. Above this the equilibria will shift off-axis, and the dipole moment will have an approximately square-root dependency on the energy. Monte-Carlo simulations agree very well with mean-field calculations; see FIG. 3.4. Near the transition energy, fluctuations in the Monte-Carlo simulations grow quite large, resembling a second order phase transition.

3.1.4 Motivation for experimentally exploring the chiral system

Bose Einstein condensates have generally been limited to relatively low vortex numbers, Smith and O'Neil's simulations were performed in the large vortex limit and agrees very well they use a minimum of 256 vortices in their Monte-Carlo simulations. Experimentally we are limited to generating on the order of 20 vortices, therefore it is unknown how well mean-field theory will model the system. The mean-field and point vortex model apply for an idealised system with no condensate, energy, angular momentum loss in a homogeneous system with no coupling to sound and perfectly hard-walls. It then poses the question of how well the mean-field theory and Monte-Carlo methods simulates an experimental chiral system. The dynamics of vortices in the chiral system also wasn't addressed by Smith and O'Neil, the relaxation time of vortices may conceivably take longer than the lifetime of an experimental condensate. Effects of non-zero, temperature, coupling to sound, the effects of impurities, and other dissipative effects are also of interest to the chiral system, as other point vortex systems in general. It is also unclear if the finite vortex number will effect the parameter space, and if vortex distributions will still be purely characterised by just energy and angular momentum. The vortices are a subsystem of the condensate that can have a negative thermodynamic temperature. While clusters are an equilibrium state for the point vortices, the condensate is still out of equilibrium, and a very interesting example of quantum turbulence.

4

Analogy to Snell's law

4.1 Reflection and Refraction of dipoles across a step-change in potential

As we have previously seen, vortex dipoles in a homogeneous condensate have straight trajectories. This implies the vortex-antivortex pair carries linear momentum, like light, and suggests an analogy to Snell's law in ray optics. Cawte et al. [29] have convincingly explored this analogy both analytically and numerically. Unlike light, the behaviour of the dipole is deterministic, and either reflects or refracts at the interface. There a set of angles close to the critical angle where dipoles are momentarily captured by the interface and travel along it.

By adapting an ansatz of the form $\sqrt{\rho(r)} = \sqrt{\rho_0} f(r)$ where $f(r) = \frac{r}{\sqrt{r^2+\xi^2}}$ is the density profile for a single vortex, it is possible to find the wavefunction for a vortex dipole, and gives a Gross-Pitaevskii energy and dipole momentum of

$$E_d = 2\pi\rho_0 \frac{\hbar^2}{m} \left[\log\left(\frac{\alpha d}{\xi}\right) \right] \tag{4.1}$$

$$P = |\mathbf{P}| = 2\pi\hbar\rho_0 d \tag{4.2}$$

Where d is the dipole separation, ρ_0 is the background condensate density, ξ is the healing length, α is $e^{(1/4+1/2)} \simeq 2.117$ analytically close to a numerical value of $\alpha \simeq 2.07$, due to differences in core structure. The speed of the vortex dipole is then given by

$$v_d = \frac{\partial E_d}{\partial p} = \frac{\hbar}{md}. \tag{4.3}$$

The dipole velocity is independent of α as long as the vortex cores are separated, as the dynamics of a single vortex is given by the local condensate density and phase. If there is a step interface between two homogeneous condensate densities, conservation of linear momentum parallel to the interface gives the Snell's law relation

$$|P_i| \sin(\theta_i) = |P_f| \sin(\theta_f). \tag{4.4}$$

Conservation of energy constrains the separation as

$$d_f = \frac{\xi_f}{\alpha} \left(\frac{\alpha d_i}{\xi_i}\right)^{\frac{\rho_i}{\rho_f}}. \tag{4.5}$$

This derivation assumes no loss of energy or momentum from acoustic waves created by the vortices at the interface. As in optics, there is a critical angle where the angle of refraction approaches 90 degrees

$$\theta_c = \arcsin\left(\frac{|P_f|}{|P_i|}\right). \tag{4.6}$$

There is a critical separation between vortices before they lose their phase windings. At this point, the two vortices become an object known as a Jones-Roberts Soliton (JRS) [53]. The JRS regime is reached when the fluid velocity between the two vortices approaches the condensate speed of sound. The topological discontinuities in phase of the vortices annihilate

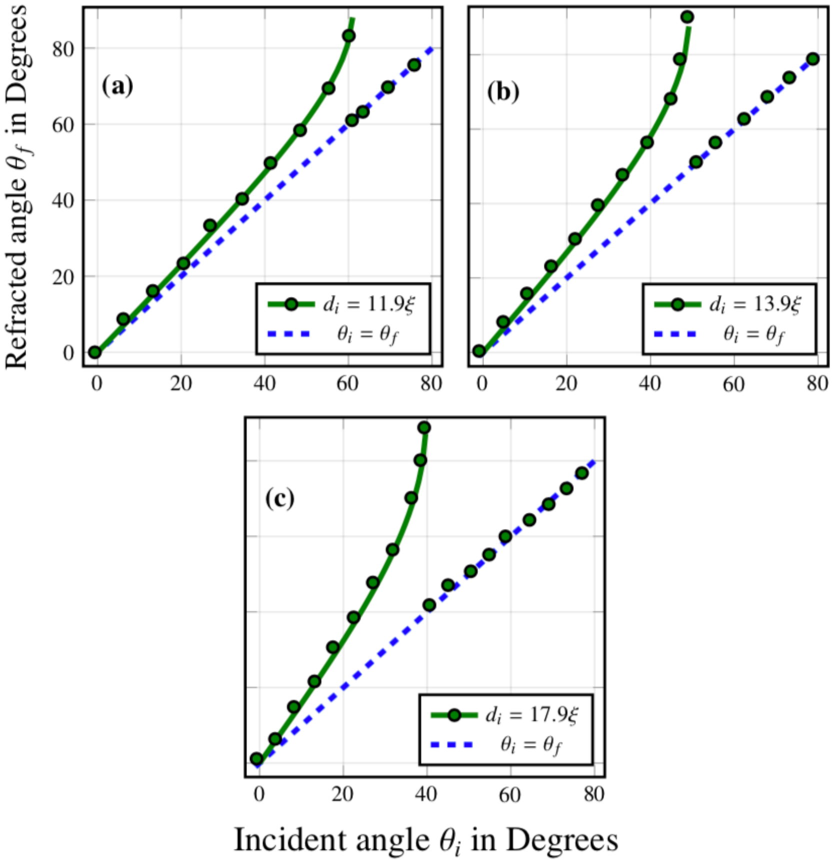

Figure 4.1: a) low density step change $\rho_1/\rho_2 = 0.95$, b) medium density step change $\rho_1/\rho_2 = 0.9$, c) high density step change $\rho_1/\rho_2 = 0.85$ Modified from [29]

leaving a π change in phase across the solition. The GPE simulations performed by Cawte et al. imprint dipoles, using the vortex ansatz, at desired positions and angles, away from a step interface in a hard walled box potential. Cawte et al. [29] show very good agreement between dipole trajectories in GPE simulations and the Snell's law relation, despite the extra complexity of the GPE. The dipole momentum is dependant on dipole separation, and affects both angle of refraction and the critical angle. The dipole separation can be viewed as analogous to the frequency or wavelength of a photon, with a dispersion relation like light travelling through a prism. Dipoles travelling from low to high densities have a set of angles close to the critical angle, where vortices are captured by the interface before either being reflected or refracted. Across high to low densities, there is no critical angle and only refraction occurs. While the vortices were imprinted in the simulations, a reliable method of vortex creation is required for generating dipoles.

4.2 On demand dipole generation using the "Chopsticks" method

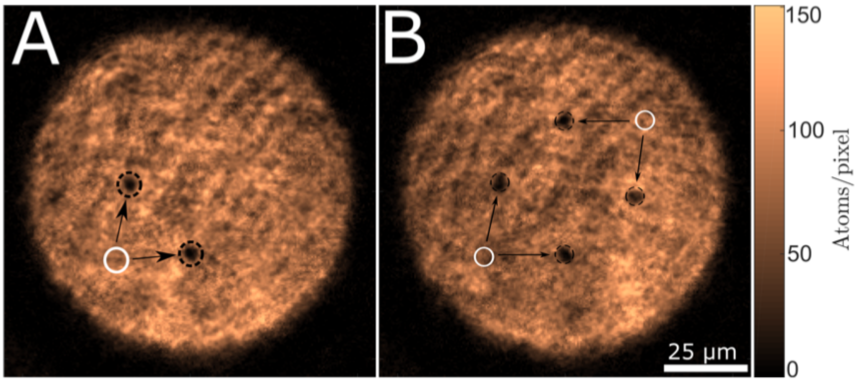

FIGURE 4.2: Scheme of creating dipoles using the chopsticks method performed in the UQ experiment [32]

By creating a blue detuned potential and splitting it into two potentials at an angle, superfluid flow, and hence vortices, becomes pinned to the potentials. Since applied potentials are easily manipulated, it is possible to move the pinned vortices around the condensate. Shrinking the pinning potential releases vortices, at a controllable initial position. This method be used multiple times in order to create somewhat arbitrary vortex configurations [54, 55].

As the pinning potentials split, a channel will open between them with superfluid filling this channel. Depending on the velocity of the pinning potential separation, the phase jump across the condensate will change. For the generation of a dipole, the phase difference will relax to 2π. For lower beam separations velocities, if the phase jump is equal to π we can create a dark soliton, another exotic excitation in the condensate, for lower beam separation velocities no superfluid current will be pinned. It is possible to create greater phase windings of $2\pi n$, where n is an integer representing the number of vortices per pinning potential, by increasing the separation velocity [54]. Multiple other methods of creating on demand dipoles exist, by sweeping either red or blue detuned potentials through the condensate [56, 57].

Using the "chopsticks" scheme with a highly oblate condensate of ^{87}Rb Samson et al. [54] were able to create vortex dipole pairs, using two blue detuned lasers to form repulsive potentials. By linearly moving the pinned pinning potentials with an angle of 66 degrees they observed reliable dipole creation in 86% of cases (out of 80), demonstrating the reliability of this method. The authors also performed numerical simulations of this system using a damped GPE, demonstrating the robustness of this scheme over a range of potential experimental parameters.

Further control over the initial positions of vortex creation can be performed by moving the pinning potentials. There are limits to this control as the vortices can become unpinned, if the pinning potentials move against the superfluid flow. Moving the potentials at velocities comparable to the Bogoliuabov speed of sound can also nucleate vortices [54, 55], similar to creating vortices by moving a potential [56, 57].

4.2.1 Motivation for a Dipole optics experiment

The UQ BEC apparatus, in principle, has the capability of creating a step change in density using the DMD and half-toning, as will be discussed in Section 5.2.1, allowing this experiment to be performed. Many investigations of vortex dynamics in harmonic and flat bottom traps has been previously made, however, the Snell's law relation has not been experimentally investigated. The physics behind this Snell's law relation is well understood, and equally applicable to Jones-Roberts solitons. An experimental demonstration of this technique would show the capability of half-toning in exploring vortex physics, showing the feasibility of vortex and soliton "optics" such as lenses. This would also allow us to probe the physics of soliton-soliton, soliton-vortex, and dipole-dipole interactions.

5

UQ experimental apparatus

The UQ BEC appartus confines a condensate of ^{87}Rb in a highly oblate trapping potential. Using a digital micromirror device (DMD), almost arbitrary optical potentials can be applied to the condensate. This makes the experiment ideal for conducting experiments on almost two dimensional superfluids. In addition to vortex experiments, this makes the apparatus well suited for atom interferometry, and atomtronics [32]. The following summarises the relevant operation of the experiment that pertain to the chiral cluster and dipole optics experiments[1].

---

[1] The experimental design has been updated over the years by a number of students under the supervision of Dr Tyler Neely. Nick Parry assembled major components, such as the vacuum system and magnetic transfer coils. Isaac Lenton was instrumental in adding the DMD. Guillaume Gauthier has made many additions, such as the field zeroing coils, and a redesign of the vacuum system. During my time on the experiment I have not designed or installed any components; however, operating the experiment, realigning optical paths, and other adjustments have comprised a significant portion of my honours project.

5.1 Optical, Magnetic and Evaporative cooling

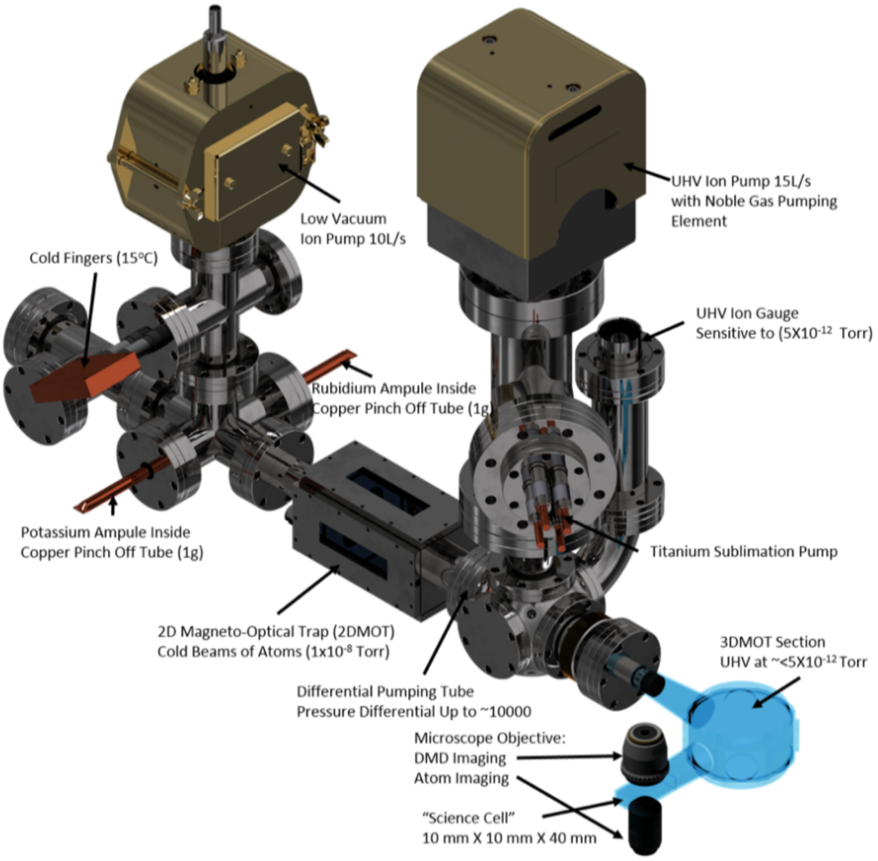
Low Vacuum
Ion Pump 10L/s
UHV Ion Pump 15L/s
with Noble Gas Pumping
Element
Cold Fingers (15°C)
UHV Ion Gauge
Sensitive to (5X10-12 Torr)
Rubidium Ampule Inside
Copper Pinch Off Tube (1g)
Potassium Ampule Inside
Copper Pinch Off Tube (1g)
Titanium Sublimation Pump
2D Magneto-Optical Trap (2DMOT)
Cold Beams of Atoms (1x10-8 Torr)
3DMOT Section
UHV at ~<5X10-12 Torr
Differential Pumping Tube
Pressure Differential Up to ~10000
Microscope Objective:
DMD Imaging
Atom Imaging
"Science Cell"
10 mm X 10 mm X 40 mm

Figure 5.1: Render of the vacuum system, comprised of the 2DMOT, 3DMOT and fused science cell. The 3DMOT is an octogon giving access to the 6 counter-propagating 3DMOT beams. The 3DMOT chamber and science cell are made from quartz and have a broad spectrum anti-reflection coating. The science cell is quite thin for cold atom experiments at 1.25mm providing close access to for optical elements, allowing commercial microscope objectives to be used [32].

The realisation that light exists in discrete energy packets or photons, that can be emitted or absorbed by atoms, was one of the first major steps towards the development of quantum mechanics [58, 59]. Linear momentum is conserved, it is possible to slow down an atom with photons. This is the principle behind optical cooling, and is utilised to cool the atoms down to the ultracold temperatures required for Bose-Einstein condensation. In the laboratory reference frame, an observer sees atomic energy transitions shift depending on the atom's velocity. This can be used to selectively excite faster atoms into higher energy states, which have a preference to drop to a lower energy level. This radiates a photon in a random direction on average slowing the atoms. This process known as Doppler cooling, can also combined with Zeeman splitting, whereby an atom's energy levels shift in the presence of an external magnetic field, to spatially cool atoms as well.

The apparatus consists of three main components, the two dimensional optical-magneto trap (2DMOT), three dimensional magneto-optical trap (3DMOT) and the quartz science cell. Atoms sublimate from a sealed 1g Rubidium sample in a copper ampoule. The atoms form a dilute vapour and are pushed along by a "zeeman slower", a laser tuned to a transition line of the atoms in the presence of a magnetic field. The atoms are moved into the 2DMOT, further cooled, before being quickly loaded into the 3DMOT. Atoms then undergo a compressed MOT stage (CMOT), where they are captured in a high 100 G/cm magnetic field. Atoms are then trapped in a quadrupole field, using two coil pairs in an anti-Helmholtz configuration, and transferred into the science cell. The field is increased and evaporative cooling occurs, where the hottest atoms are allowed escape from the magnetic trap. Atoms in the $|F = 1, m_F = -1\rangle$ magnetically trappable state are selectively excited, with microwave frequencies, to the $|F = 2, m_F = -1\rangle$ non-magnetically trappable state. The atoms are then loaded into a hybrid optical magnetic trap, provided by a red detuned (1064 nm) laser sheet. The atoms are then lowered into a red detuned sheet and evaporatively cooled, by reducing the power of the optical trap. Finally creating condensates of approximately 4×10^6 atoms at a condensate fractions of 80%.

During this process, care must be taken to ensure no vortices are generated due to the Kibble-Zuruk mechanism, where fast evaporation leads to topological defects in the phase of the condensate [60, 61]. It is also important to ensure that the red detuned sheet is as smooth as possible, as interference fringes in the sheet occur from back reflection from the science cell. Large fringes in the red sheet can cause condensate flows as the red sheet power is lowered, nucleating vortices.

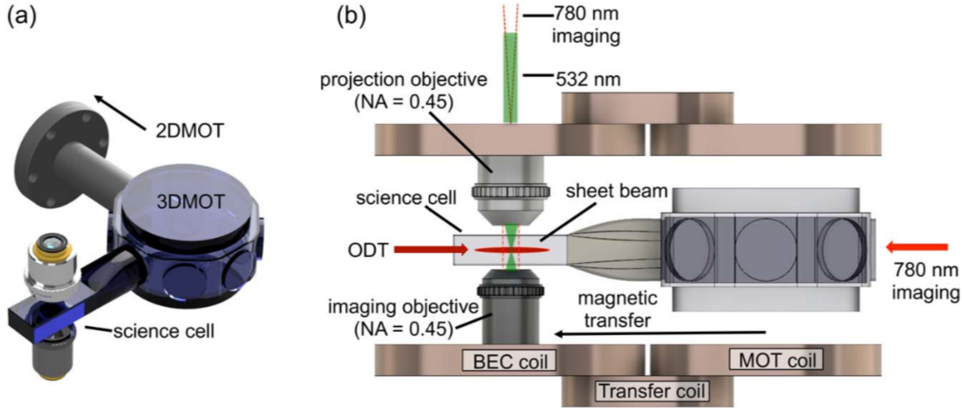
(a)
2DMOT
3DMOT
science cell
(b)
780 nm imaging
projection objective (NA = 0.45)
532 nm
science cell
sheet beam
ODT
780 nm imaging
imaging objective (NA = 0.45)
magnetic transfer
BEC coil
MOT coil
Transfer coil

FIGURE 5.2: Details of the 3DMOT chamber and science cell. From the 3D magneto optical trap, the atoms are in the $|F = 1, m_F = -1\rangle$ magnetically trappable state and transferred to a magnetic trap provided by the MOT coil. Transfer coil moves the atoms into another magnetic trap generated by the BEC coil. After microwave evaporative cooling, the atoms are loaded into a hybrid magnetic optical dipole trap (ODT), 1064 nm red detuned sheet, and undergo further evaporation. They are then transferred into another optical dipole trap with optical trapping in the x-y plane by (532 nm) blue detuned light projected from the digital micromirror device (DMD) [62]. Not shown in this diagram is the custom 3D printed side zeroing coil assembly used to cancel stray magnetic fields.

5.2 Optical control using the digital micromirror device (DMD

As optical fields are highly controllable, they allow the creation of configurable potentials. Spatial light modulators (SLMs) are a common method for creating trapping potentials in atomic optic experiments. A increasingly common method, in cold atom experiments, is the use of a digital micromirror device (DMD), an array of individually controllable mirrors, pioneered by the UQ experiment. DMDs offer high spatial resolution and fast refresh rates of approximately 20 kHz. The relatively thin glass cell walls the experiment allow high resolution, low focal length, optics to be used for both applied potentials and imaging. The DMD projects blue detuned 532nm light onto the atoms trapped in the red sheet. The resolution of the experiment between that of atomic microscope experiments and and more traditional BEC experiments.

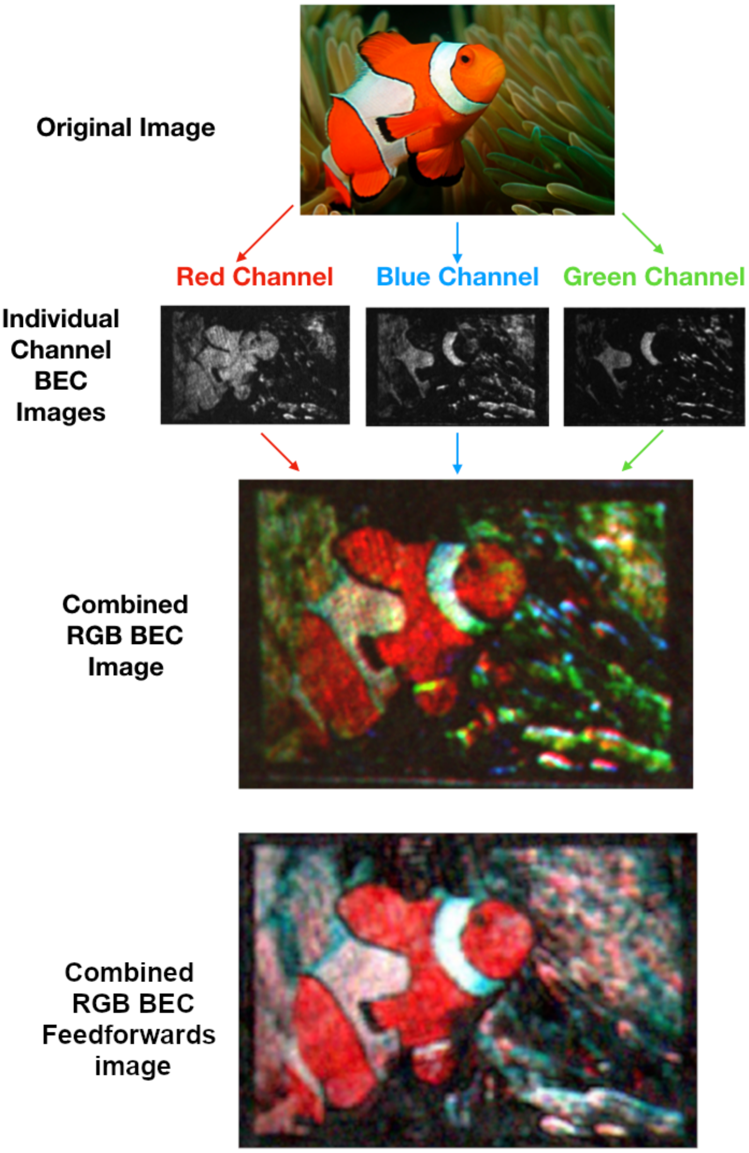
Original Image
Red Channel
Blue Channel
Green Channel
Individual Channel BEC Images
Combined RGB BEC Image
Combined RGB BEC Feedforwards image

Figure 5.3: To demonstrate the abilities of DMD half-toning it is possible to create a combined RGB image using the DMD. Here we take a potential based off a colour channel of an image (red, green and blue), then use it to contain the atoms as the groundstate of the wavefunction in the Thomas Fermi approximation assumes the state of the potential $n = \Psi^2 = (\mu - V_{ext})/g$. This creates images of each of the individual channels. When all three are combined it creates a colour RGB image. This can be further improved using the feedforward method to create a smoother condensates. This method allows us to use the BEC as a new artistic medium.

5.2.1 Half-toned optical potentials using the Floyd-Steinberg dithering algorithm

While the mirrors in the DMD can only form a binary pattern, light from a single mirror will diffract. The size of the illuminated spot from a single mirror is given by the point

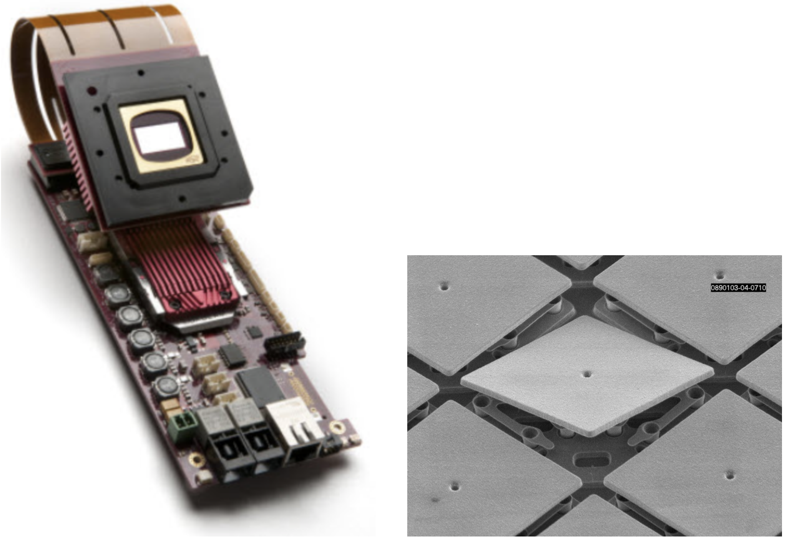

FIGURE 5.4: a) the Visitech LUXBEAM 4600 DMD used the in experiment, with a total of (1200×1900) mirrors. DMD controller has on-board storage of up to 13,889 frames, and a refresh rate of $20,000$ Hz [63]. b) single mirror activation on a DMD [64]. Due to diffraction from individual mirrors the size of a spot illuminated by a single mirror will have FWHM of 630(10) nm. This is smaller than the individual mirror size. As the individual spots created by the mirrors will overlap, it is possible to create applied laser intensities between 0 and the maximum laser intensity 5μ. This is performed using an error diffusing (dithering) algorithm and has the ability to create smooth almost arbitrary potentials. [62]

spread function, which has a 630(10) nm full width half maximum (FWHM) on the atomic plane. The optical potential in the atomic plane from the projected light is a convolution of the binary mirror pattern and the PSF, resulting in a smoothed projected pattern. From the binary mirror pattern, apparent shades or “half-tones” that will be smoothed due to diffraction, can be created with the use of a dithering algorithm, based on the Floyd-Steinberg algorithm. This is an “error-diffusion” algorithm that assigns an error based on the difference between a pixel and desired shade, and propagates spreads this error to the surrounding pixels determining the binary value of a pixel [65]. The suitability for dithering a DMD in cold atom experiments was shown by Liang et al. [66]. This allows for near arbitrary potentials to be applied to a BEC. We have demonstrated the capability of the experiment by creating replicas of artworks, such as the Mona Lisa and Starry Night, on a quantum canvas. Furthermore by splitting a colour picture into its red, green, and blue component channels, it is possible to make colour BEC patterns.

5.2.2 Feedforward method of creating desired potentials

While the dithering method works relatively well, aberrations and foreign particles, such as dust, in the optical path of the DMD obscure the projected blue detuned light, causing imperfections in the applied potential. In order to correct for these aberrations, it is possible to modify the DMD pattern, using either an image of the projected light, or an image of the condensate. In practice we create an error-map, from the difference between the condensate density and desired density. The error-map is then feedforward, by switching mirrors on or off proportionally in proportion to the difference. In areas of lower than desired density, mirrors are turned off, lowering the applied potential and visa versa, converging the condensate density to towards a desired profile. Unfortunately there are also aberrations in the imaging path of the experiment which has the affect of adding false corrections. It is very difficult to tell whether a condensate in reality is smooth, or if only the image of the condensate is smooth [32, 62].

5.3 Imaging

In order to check the alignment of the system, the number of atoms in the condensate number, and fraction of condensed atom, side imaging is required. Under expansion free of external potentials the atomic cloud will expand (and simultaneously fall due to gravity). Two distributions will emerge, the tightly peaked Bose-Einstein distribution of atoms in the groundstate, and a broader thermal distribution. Numerical integration of these distributions gives the number of condensed atoms, and atoms in the thermal cloud, and hence the condensate fraction. Side imagine is was captured using a PROSCILICA camera. The thin glass walls of the science cell allow a high numerical aperture NA = 0.45, low focal length lens to be used for vertical imaging. This offers high resolution imaging with a resolution of around $600nm$ slightly greater than the vortex healing length. This images atoms in the x-y plane, and was used to take all of the experimental data presented in this thesis. Due to the short focal length, care was taken to ensure that the atoms were in focus.

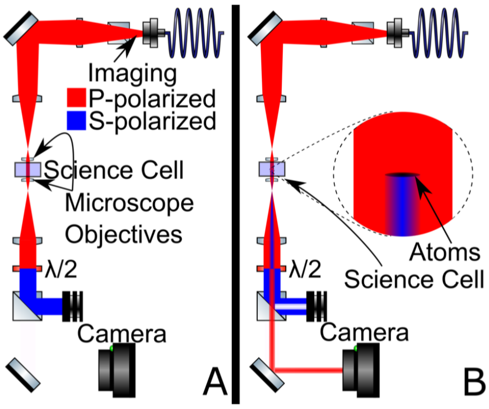

FIGURE 5.5: Scheme of Faraday imaging A) Light travelling through the science cells without the presence of atoms doesn't change polarisation, and is dumped. B) Light travelling through atoms picks up some phase, and isn't dumped by the halfwave plate, showing the density of the atoms [32].

Absorption imaging is the simplest and most common imaging scheme for cold atoms. An applied (780nm) imaging beam absorbed as it passes through atoms, resulting in a shadow of the atomic cloud. This is subtracted from an image without a condensate, to give the density of the atoms. Imaging is performed on the $5^2S_{1/2}\,|F=2\rangle$ to $5^2P_{3/2}\,|K'=3\rangle$ transition line, which requires the atoms to transferred from the $|F=1\rangle$ to the $|F=2\rangle$ state immediately prior to imaging.

Faraday imaging relies on change of polarisation as the imaging beam passes through the atomic cloud. This is more sensitive to density fluctuations than absorption imaging, so it is the preferred method of imaging vortices and used for all the data presented in this thesis.

Vortex Detection Algorithm

It is also possible to locate the positions of vortices from images of the condensate density using a Gaussian blob detection algorithm. This takes the Laplacian of a smoothed image, as vortices change the density of the condensate these will appear as "blobs", a threshold is applied to the Laplacian and position of the "blobs" are found by fitting Gaussian distributions to them [13]. There is some error in the algorithm, where false vortices are detected and some vortices are ignored, however it is still relatively accurate. This method is relatively robust, however the smoothing, and threshold values need to be adjusted occasionally to improve the vortex fitting.

6

Experimental observations of Onsager Clustering in the Chiral system

In this chapter we present an experimental study of equilibrium states of the chiral system, as was investigated by Smith and O'Neil [19], and discussed in Chapter 3. While other papers have experimentally investigated the behaviour of a system of vortices and anti-vortices notably Jonestone et al. [14] and by Gauthier, Neely et al. [13], the chiral system has not been experimentally investigated. The chiral system is more attractive in many ways, opposed to the two-signed system, as the vortices cannot annihilate one another, so vortex loss is lower and cluster stability is higher. Initial vortex cluster states can be deterministically injected into the condensate by the use of optical paddles sweeps, which allows equilibrium and non-equilibrium clusters to initially created. We observe both on on-axis and off-axis vortex cluster equilibrium states, as well as the relaxation of an initially non-equilibrium state. The experimental data is very well modelled by GPE, dynamic point vortex, and Monte-Carlo point vortex simulations. In particular this allows us to probe the parameter space and address the question of how long a non-equilibrium state takes to thermalise into an equilibrium state.

6.0.1 Vortex injection methods and 2D GPE simulations

In order to observe the axisymmetric and non-axisymmetric states predicted by Smith and O'Neil [19], it was necessary to use repeatable deterministic vortex nucleation techniques. It was decided to create equilibrium vortex clusters centred on-axis, off-axis and well as a non-equilibrium state. We should note that the previous work of Gauthier, Neely et al. [13] does not address the relaxation of non-equilibrium states or probe the parameter space of the vortex system. The non-equilibrium state was chosen to be two off-axis clusters mirror symmetric clusters. From mean-field theory and Monte-Carlo simulations we expect this to relax into an off-axis cluster (due to its relatively high angular momentum). However, the time required for this to occur in a real system was unknown. While the choice of a non-equilibrium initial state is arbitrary, the two cluster initial state has a dipole moment close to zero ie. the average vortex position lies at the centre of the trap. The dipole moment is a measure of the distribution of the vortices and hence the symmetry of the system.

As we are generating single signed vortices, they must be introduced via the boundaries of the fluid due to their topological nature. The vortex injection methods all rely on optical paddles swept through the condensate using the dynamic capacity of the DMD. This was performed over 200 frames leading to a approximately smoothly time varying potential, analogous to sweeping paddles through water. In order to ensure that these methods only inject a single signed vortex, and leave the condensate density otherwise relatively homogeneous, a dimensionless simulation of the damped GPE, of damping factor $\gamma = 5 \times 10^{-4}$, was performed, as discussed in Appendix A. These were performed on $(400, 400)$ lattices with a width of 120ξ, and externally applied potential trap or radius 100ξ, closely matching the experiment. The simulations were run for $20,000\tau$, or approximately $7.7s$ in a real system, and sampled every 10τ, or $4ms$. While the simulated parameters are close to that of the experiment, small variations in the size, shape and velocity of the paddles can greatly change the density and number of vortices in their initial cluster. . Finding vortex injection methods that created tight vortex clusters with adequate vortex numbers that were repeatable was time consuming experimentally and numerically.

Simulations provide insight into the behaviour of the system dynamically, compared to experimental images which are destructive and require a new experimental run for every image. Bragg imaging, which could have detected the velocity field of the condensate, was not performed for this system [13]. The simulations give confidence that the vortices are all same signed and that sound waves and solitons are absent from the initial vortex state. The qualitative agreement between point vortex simulations and the data provides confidence in the preparation of the initial state. Slight changes in condensate density and the presence of sound could change the number of nucleated vortices from experimental sweeps using these methods, however the clusters have been observed to be relatively consistent in their number and location.

The distributions of the vortices, and hence the dipole moment, are statistical and require multiple simulations to find their behaviour. This requires unnecessary computational effort compared to the simple point vortex model, which allows us to capture adequately capture much of the physics with far less computational cost.

Centre Pinning (on-axis cluster)

Vortices can captured or pinned by an potential in the condensate. As the condensate density is lower, the flow fluid induced by a vortex is lowered, and the vortex energy is reduced. This can alternatively be thought of as pinning superfluid flow around a potential, similar to the use of chopsticks in Chapters 4 and 7. The use of a central pinning potential is used to create initially on-axis clusters. This was done with a pinning site with radius of 30ξ, or around $15\mu m$ experimentally. In order to create superfluid circulation around the pinning potential, a paddle of width 4ξ or $2\mu m$ was extended radially from the pinning potential

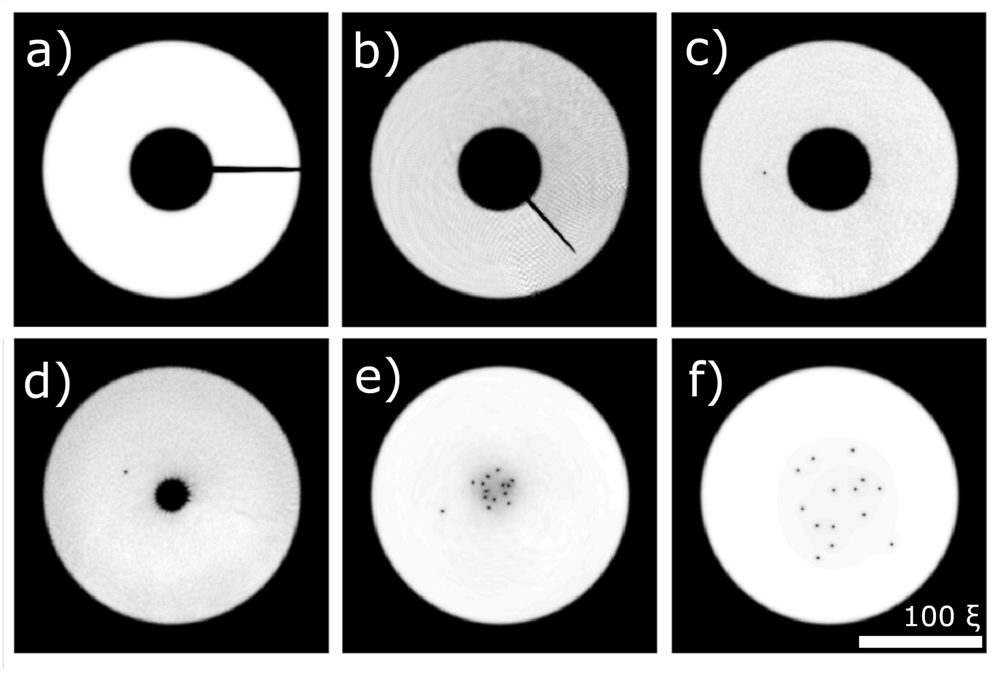

Figure 6.1: On-axis vortex cluster injection simulation using the unitless 2D GPE with numerical damping term $\gamma = 5 \times 10^{-4}$. Images are shown at times a) 0τ (0 s), b) 500τ (0.19 s), c) 1000τ (0.38 s), d) 1100τ (0.42 s), e) 5000τ (1.92 s), and f) 20000τ (7.70 s). This is the system in the top row of Fig. 6.5

to the boundary and rotated around the centre of the trap. The paddle was removed by shrinking it into the central pinning potential, in order to leave a total of 13 quanta of rotation around the pinning potential. During the retraction a single vortex of the same sign was left within the condensate, matching experimental images which often have an extra vortex outside of the cluster. See Fig. 6.1 for details of the simulation. The presence of a single extraneous vortex has little effect on the behaviour of the central cluster. A damping factor of $\gamma = 5 \times 10^{-4}$ was used in this simulation resulting in a qualitatively wider spread of vortices than observed experimentally.

Single Sweep (off-axis cluster)

After some experimentation using rotational paddle sweeps and moving vortices trapped on a pinning potential, it was found that the most reliable way to generate a single cluster of off-axis vortices was to linearly sweep a paddle through the condensate. The paddle has width 4ξ or $2\mu m$ and travels through the condensate at a velocity of $0.2c$. The paddle is

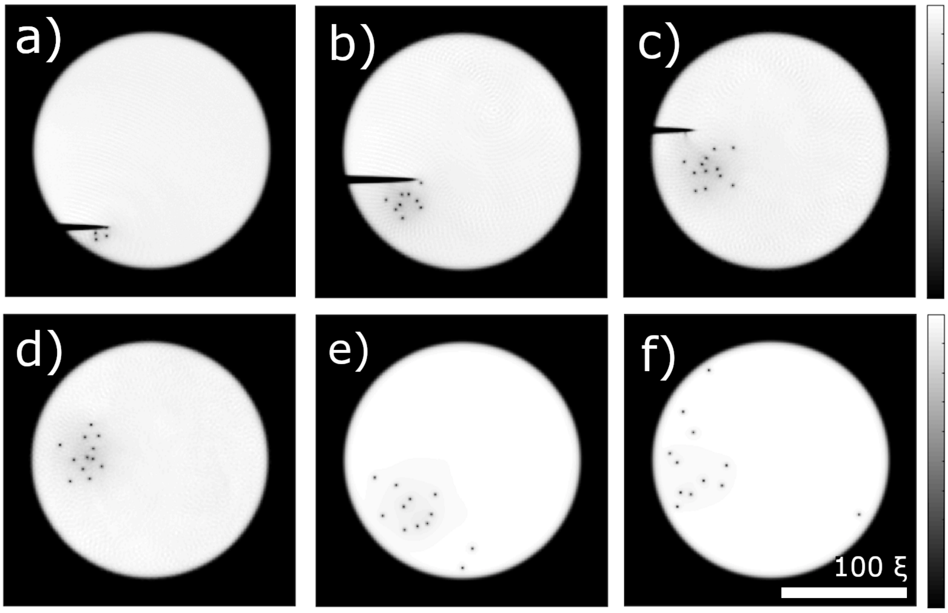

Figure 6.2: Off-axis vortex cluster injection simulation using the unitless 2D GPE. This simulation uses numerical damping term of $\gamma = 5 \times 10^{-4}$. Images taken at times a) 200τ (0.077 s), b) 400τ (0.15 s), c) 600τ (0.231), d) 1000τ (0.39 s), e) 10000τ (3.85 s), and f) 20000τ (7.7 s). This is the simulation in the middle row of Fig. 6.5

withdrawn as it passes halfway through the trap. This generates 12 vortices in an off-axis cluster. After vortex nucleation the off-axis cluster stays in an off-axis cluster for the duration of the simulation. See Fig. 6.2.

Double Sweep (non-equilibrium state)

Similarly to the single paddle case, two paddles can be swept through the condensate at a velocity of $0.15c$, generating two highly symmetric clusters with 7 vortices each. Unlike experiments, there is a high degree of symmetry in this system, resulting no off-axis cluster transition, as the damping factor $\gamma = 5\times10^{-4}$ removes any noise that would break symmetry. With zero damping $\gamma = 0$, the off-transition occurs much later than seen in the experiment, at around 17000τ, much later than that observed experimentally transition at $2s$ or 5200τ.

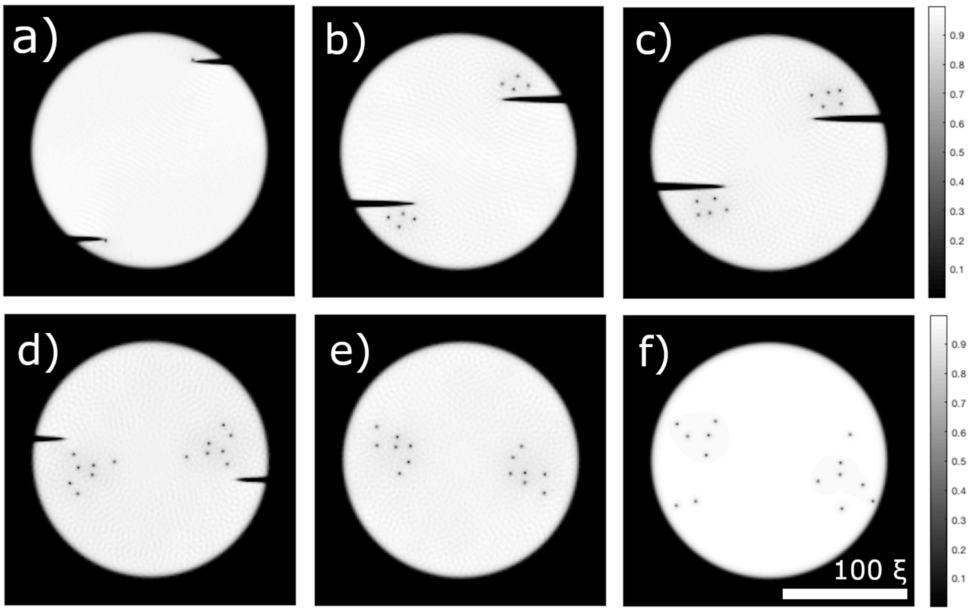

FIGURE 6.3: Two vortex cluster injection simulation using the unitless 2D GPE. This simulation uses numerical damping term of $\gamma = 5 \times 10^{-4}$. Images taken at times a) 200τ (0.077 s), b) 400τ (0.15 s), c) 500τ (0.19s), d) 800τ (0.30 s), e) 1000τ (0.39 s), and f) 20000τ (0.77 s). Interestingly for this simulation, the dipole moment is almost zero for the entire simulation as the two clusters never merge, due to the simulations high degree of symmetry. This is the simulation in the middle row of Fig. 6.5

6.0.2 Equivalence between GPE simulations and the point vortex model

As a demonstration of the agreement of the GPE and the point vortex model, it is possible to create the phase of the condensate using $\theta = \sum_i \operatorname{atan2}(y - y_i, x - x_i)$. The behaviour of the vortices is only dependant on the local phase and density of the condensate (as discussed in chapter 3) so as long as the vortices are separated further apart than a couple of healing lengths the structure of the vortex cores have no significant impact on the vortex dynamics. It is also worth noting that while the density and phase of the condensate does not appear to resemble the flow of a classical fluid, such as a cyclone or soap film, the velocity field bares a qualitative resemblance, as can be seen in Fig. 6.4, as demonstration of link between quantum turbulence and classical two dimensional turbulence. This also demonstrates the feasibility of imprinting point vortices onto the condensate, by applying this phase and the vortex density anstaz $n(x) = r/sqrtr^2 + \xi^2$, to an initial wave function and evolving it in

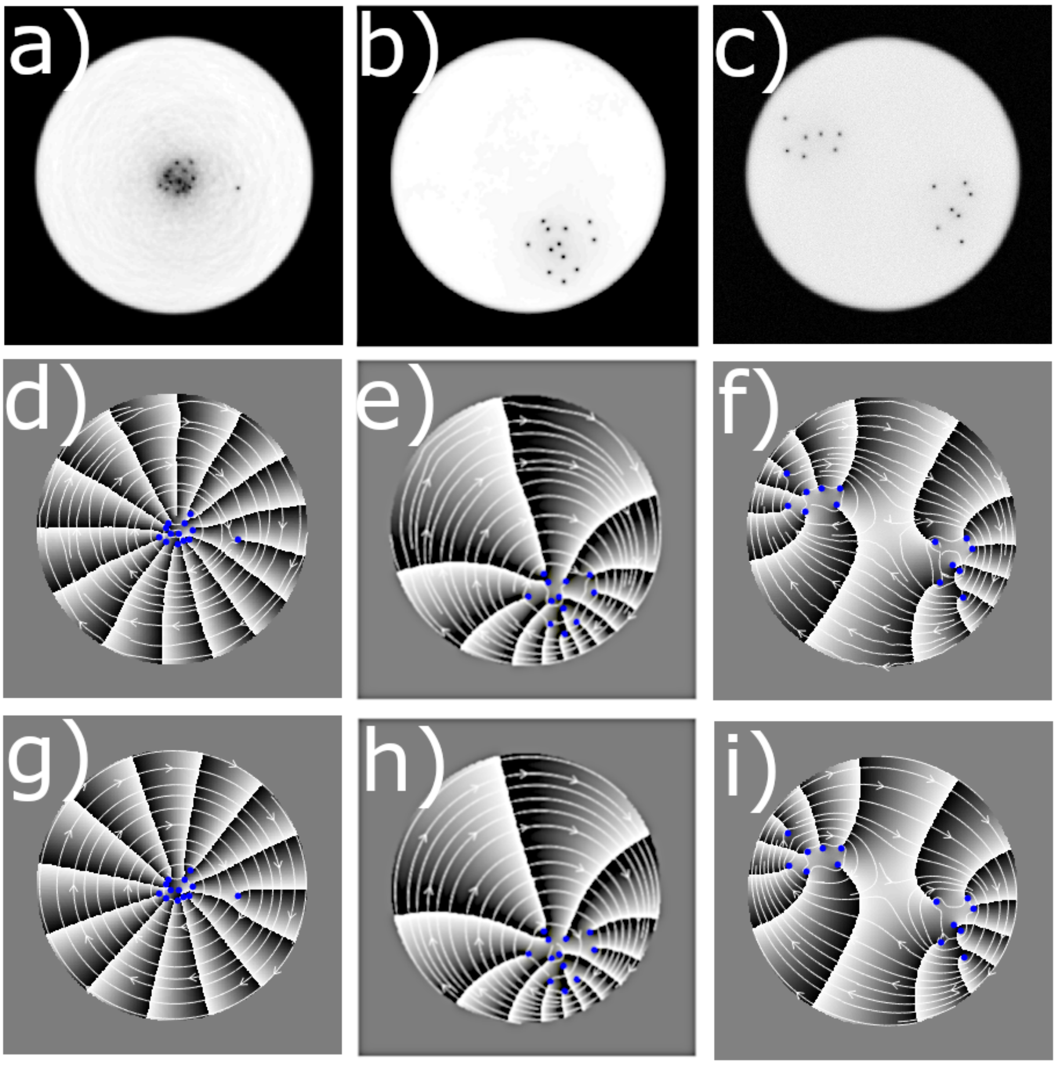

Figure 6.4: Comparison of the point vortex model and the GPE, for the on-axis cluster, left, the off-axis cluster, middle, and non-equilibrium state, right. The top row displays the GPE densities. Middle row, the GPE phase, velocity field and marked point vortex positions. Bottom row has the phase generated by point vortices, $\theta = \sum_i \arctan((y - y_i)/(x - x_i))$ (where the sum is over the positions of all the vortices and image vortices), where the position of the vortices has been taken from the GPE simulation, and velocity field from the point vortex phase. Notice while the GPE and point vortex phases agree well, very subtle differences in phase between the GPE and PV models due to the presence of soundwaves and extra excitations in the condensate.

time.

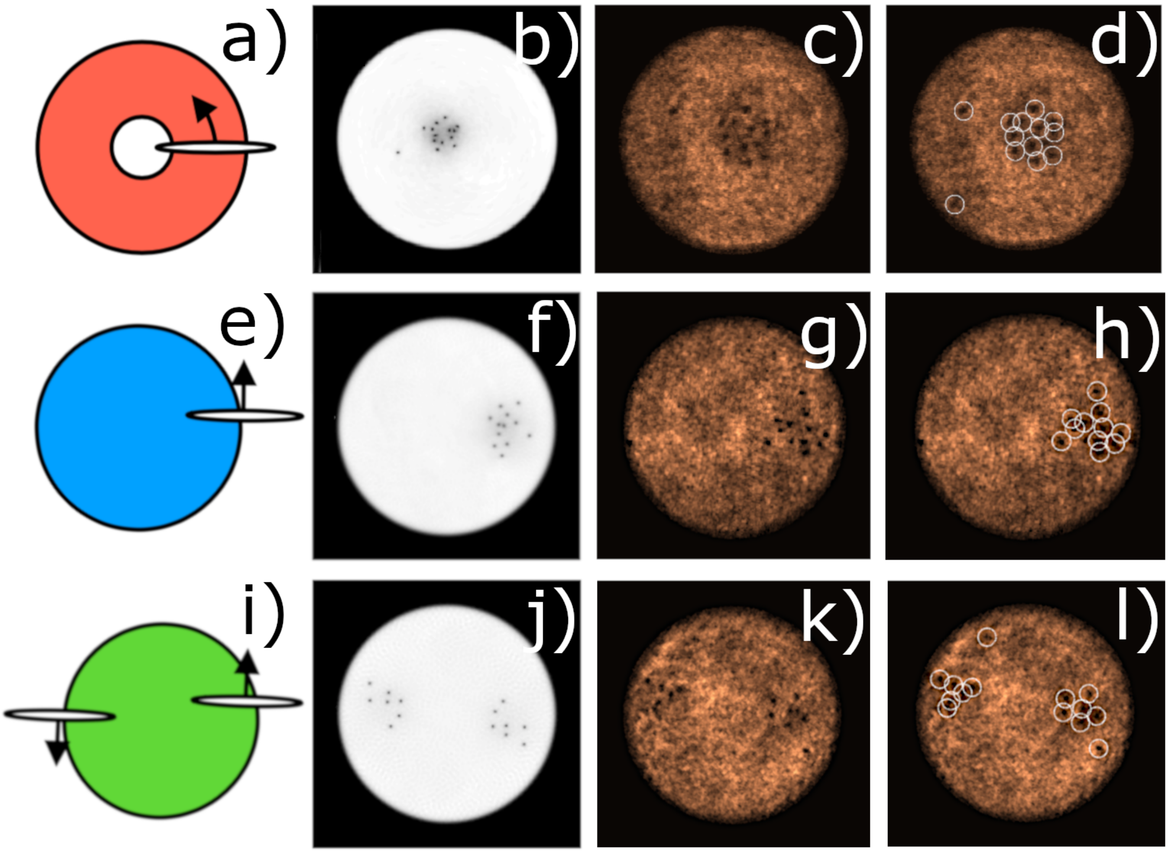

FIGURE 6.5: DMD paddle sequences, simulated initial vortex positions, experimental vortex positions and detected vortex positions: from left to right. Centre pinning a)-d) creates axisymmetric vortex clusters; note the absence of an extra vortex in the example experimental data. Single sweep e)-h) creates off-axis vortex clusters. Double sweep i)-l) creates two off-axis clusters with mirror symmetry.

6.1 Experimental results

Condensates of around 4×10^6 atoms were formed in the red detuned (1064 nm) highly oblate sheet with a trapping frequency of $(\omega_x, \omega_y, \omega_z) = 2\pi(1.8, 1.6, 106)$. Extra trapping in the x-y plane was applied with blue detuned (532 nm) laser light reflected from the DMD with a trap depth of around 5μ. The DMD trap was used to create a circular trap with a diameter of $100\mu m$. This is nearly a hardwall potential with some roll-off, due to the PSF with a HWHM of $650nm$. The resulting condensate in this potential is relatively homogeneous, as can be seen in the experimental figures. The condensate has a healing length of approximately $\xi = 500nm$, in the centre of the trap and a Thomas-Fermi diameter of

$6\mu m$ vertically resulting in a Bogoliubov speed of sound of $1290\mu m/s$. Care was taken to ensure that magnetic fields across the condensate were cancelled with the side zeroing coils, using the position of a centred cluster of vortices. As the vortex size is on the order of the healing length around the resolution limit of the imaging system, a brief 3 ms period of free expansion is performed before imaging, known as time of flight (TOF).

We took 40 sets of data for the centre pinning, 49 sets of data for the single sweep and 41 sets of data for the double sweep. Each set consists of images, taken 250 ms apart, from 0 to 6.75 s, so each set of time series data consists of 28 images. This comes to a total of 1120, 1372, and 1148 images respectively for the various initial conditions. We see good qualitative agreement between the GPE simulations and the experimental data, for the initial nucleation of vortices. We also see a relatively homogeneous condensate without the presence of solitons, or other discernible large soundwaves. Much of the inhomogeneities in the images come from imaging artefacts such as dust and other aberrations in the imaging system.

6.2 Mapping experimental data onto Point Vortex Model

By measuring the vortex positions with the Gaussian Blob detection algorithm [13], see Section 5.3, it is possible to measure the vortex number and identify vortex positions, see Fig. 6.5 for examples of the vortex detection algorithm in action. It is then possible use these detected positions to map back onto the point vortex model in order to extract the energy, angular momentum and dipole moment, as presented in Section 2.2.1. The energy is

$$H = -\frac{1}{4\pi}\sum_{i\neq j}\Gamma_i\Gamma_j \ln\left|\frac{\mathbf{r}_i-\mathbf{r}_j}{R}\right| - \frac{1}{4\pi}\sum_{i,k}\Gamma_i\Gamma_j \ln\left|\frac{\mathbf{r}_i-\bar{\mathbf{r}}_k}{R}\right|, \tag{6.1}$$

the angular momentum is

$$M = \frac{1}{2}\sum_{j=1}^{N}\Gamma_j r_j^2. \tag{6.2}$$

and dipole moment of

$$D = \sum_i s_i x_i \hat{i} + \sum_i s_i y_i \hat{i}.$$

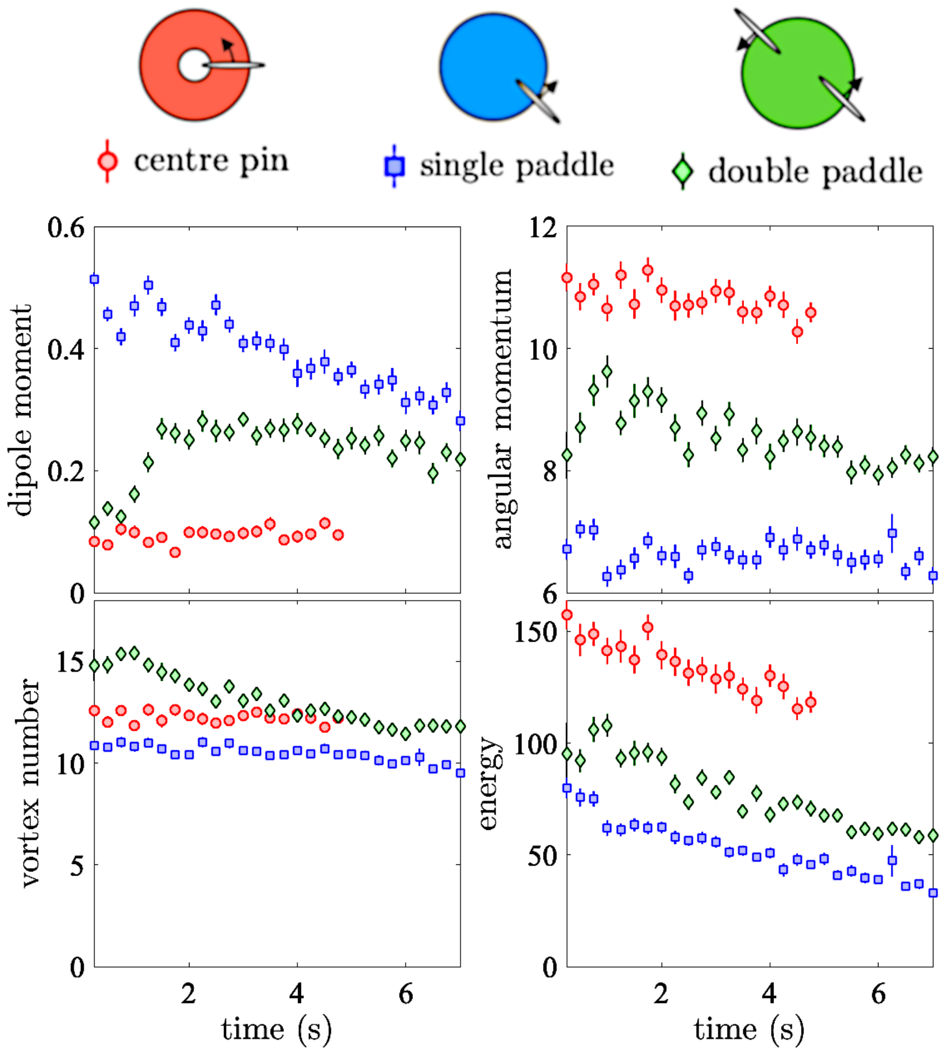

FIGURE 6.6: Experimentally found point vortex number, energy, angular momentum, and dipole moment. These were found by finding vortex positions using the vortex-detection algorithm, and the point vortex model. These experimental results will be compared to a number of simulations

6.2.1 Imprinted vortices in a dynamic GPE simulation

Using the experimentally found vortex positions, it is possible to imprint vortices at arbitary locations in the condensate by taking the Thomas-Fermi approximation for the groundstate, and using the Ansatz for the local density around a vortex $n(\mathbf{r}) = \dfrac{|\mathbf{r}-\mathbf{r_i}|}{\sqrt{|\mathbf{r}-\mathbf{r_i}|^2+\xi^2}}$, and the phase $\theta = \sum_i \operatorname{atan} 2(y-y_i, x-x_i)$, generated by these vortices. Due to the computational time involved with performing a GPE simulation, only a single initial experimental configuration was used to simulate an experimental run. Surprisingly even with just a single

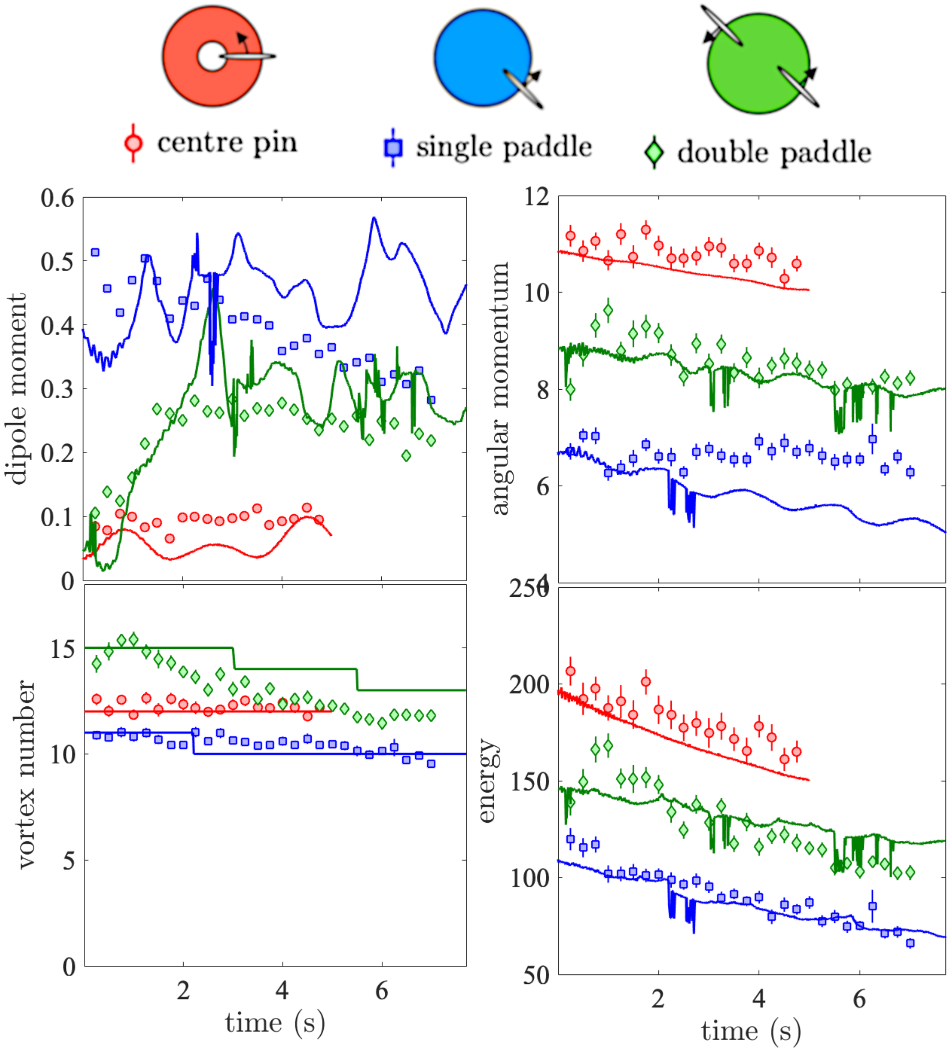

Figure 6.7: A single trajectory of imprinted vortices (marked with a solid line), based on experimental positions, using the GPE compared to experimental data. Qualitatively these appear to relatively well match the vortex number, energy, angular momentum and dipole moment, which some variation due to the vortex-detection algorithm, playing up with vortices leaving the condensate. Due to the computational requirements of the GPE, it wasn't feasible to simulate every initial vortex distribution using the GPE. The trajectory of the vortices using the GPE should be compared to the trajectory of vortices in the dynamics point vortex model, shown in Fig. **??**.

trajectory, the GPE simulation data appears to fit the experimental data rather well. This potentially shows that simulations of the GPE are good enough to simulate the experiment, however the average of many simulations is needed to show this, requiring some fine-tuning of the damping parameter.

6.2.2 Dynamic Point Vortex Model

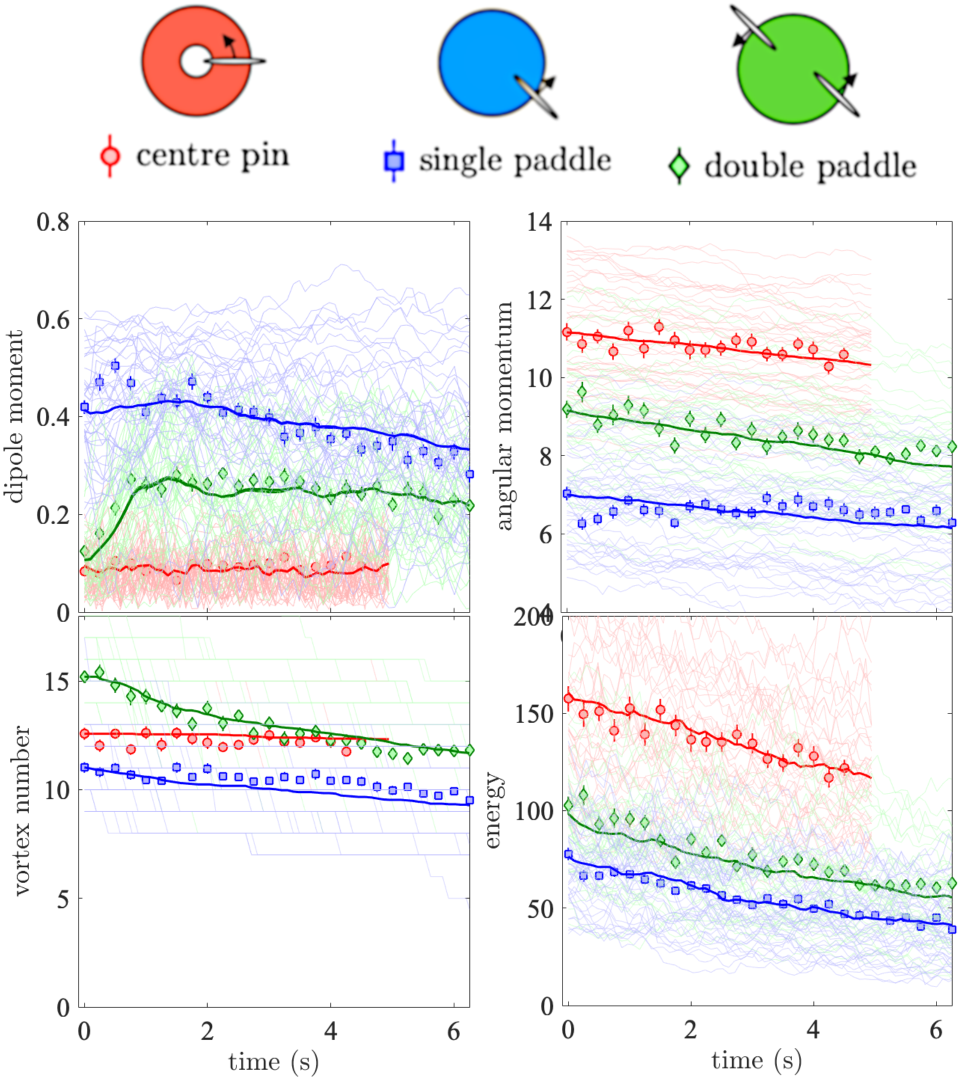

FIGURE 6.8: Plots of the dipole moment, angular momentum, vortex number and energy over time. The red and blue plots are the single on-axis and off-axis clusters respectively, which evolve smoothly over time. The green plot is that of the two cluster case which quickly equilibrates into a single off-axis cluster as can be seen in the dipole moment. The markers represent experimental data, while the solid lines are point vortex simulations based on the initial vortex distributions

It is possible to take the the measured experimental vortex positions, and evolve them in time using a modified point vortex model.

$$\kappa_i x_i = \frac{\partial H}{\partial y_i}\,\mathrm{d}t + \sqrt{\eta}\,\mathrm{d}W_x\,, \tag{6.3}$$

$$\kappa_i y_i = -\frac{\partial H}{\partial x_i}\,\mathrm{d}t + \sqrt{\eta}\,\mathrm{d}W_y\,, \tag{6.4}$$

where H is the Hamiltonian, given by Eqn. 6.1, with $\mathrm{d}W$ a Gaussian noise term with unit variance. Vortex annihilation is taken into account by removing vortices within a numerically enforced vortex core size ξ of the boundary, where the core size is chosen to be the healing length. A point vortex model has no dissipation, so energy, vortex number and angular momentum are conserved, and has to be modified to include damping seen in real systems, see Fig. 6.6. A damping term γ, analogous to the phenomenological damping term in the GPE, is typically used in point vortex simulations but this damping term poorly modelled the dipole moment. It was found that a Brownian motion term better fit the experimental data. The term $\sqrt{\eta} = 2 \times 10^{-2}$ was found to fit the data for all three cases. While it might seem counter-intuitive that the noise term would cause dissipation, one could consider a random walk of a vortex within a cluster. As there are more ways, on average, for the vortex to leave the cluster than to remain, the vortex separation will on average increase with time reducing the energy. Similarly, there are more ways for the vortex to walk towards the edge of the condensate than towards the centre, on average decreasing the angular momentum.

While the extra Brownian motion term in the point vortex model accurately captures the dynamics of the vortices it is unclear why it works so well, especially compared to the imprinted GPE simulations. A comparison between the experimental data and a more realistic PGPE or SPGPE simulation may be quite informative in this regard.

6.3 Thermalisation and Demon Monte-Carlo

We can interpret the vortex equilibria positions to be the result of the cluster equilibrating at some temperature. As the total energy and angular momentum decrease over time, this equilibrium state relaxes. We perform a demon Monte-Carlo simulation following the technique of Smith and O'Neil.

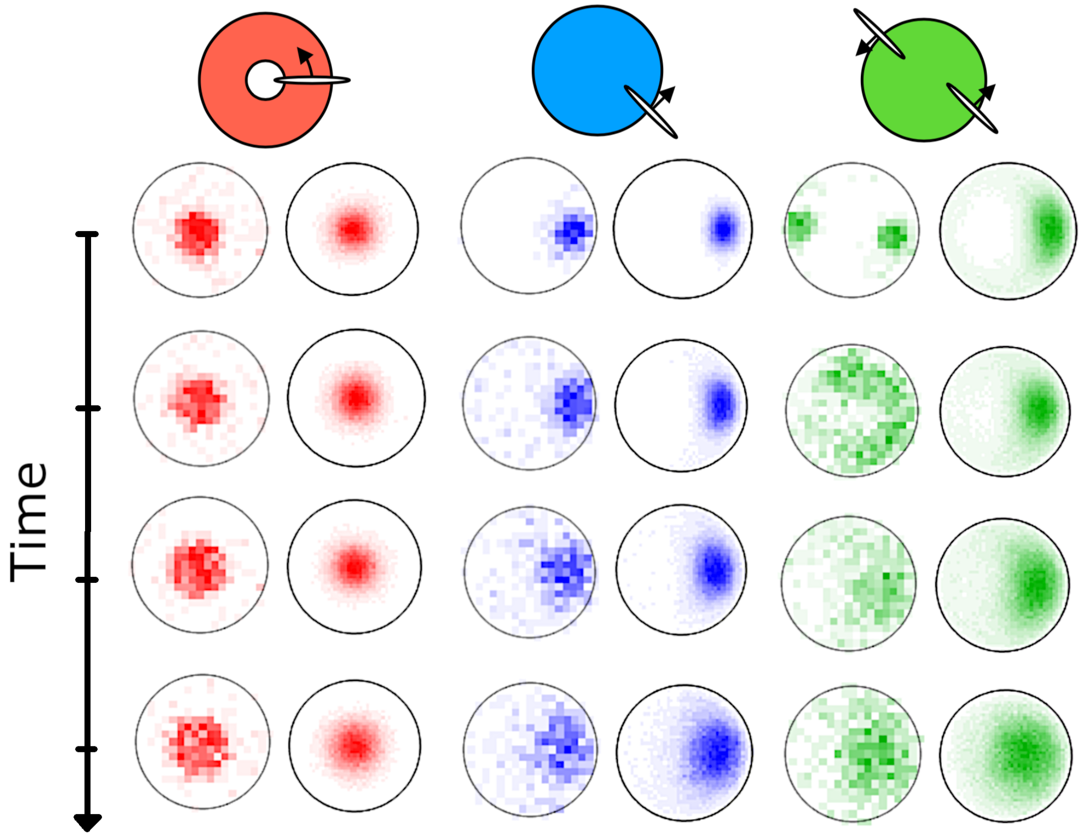

FIGURE 6.9: Clustering Histograms on the left from measured vortex locations at times $t = 0$, $t = 1$,$t = 2.5$, $t = 6.75s$, compared to histograms from Monte-Carlo ensembles on the right. Clearly the experimental data matches the Monte-Carlo simulations well for the on-axis and off-axis initial conditions. For the non-equilibrium initial condition of the two cluster state, the vortices start in two clusters but relax into equilibrium over a short time-frame, see Fig 6.11 to see the dipole moment of the data match that of the Monte-Carlo simulations. This demonstrates that the two clusters have reached equilibrium. For all the histograms, except for the initial state of the two cluster system, the vortex locations have been rotated such that their dipole moment lies on the x-axis.

Core Repulsion

The dipole moment from this simulation is a little below of the dipole moment from the experiment. The reason for this is it takes a lot of energy for two vortices to cluster due logarithmic term in the Hamiltonian, Eqn. 6.1. The vortices want to distribute the energy between them as much as possible, so in a real system its quite rare for vortices to be within a few healing lengths of one-another, as we see from histograms of experimental vortex nearest neighbour distances, no vortices cores are within 5 μm of another. A Monte-Carlo demon

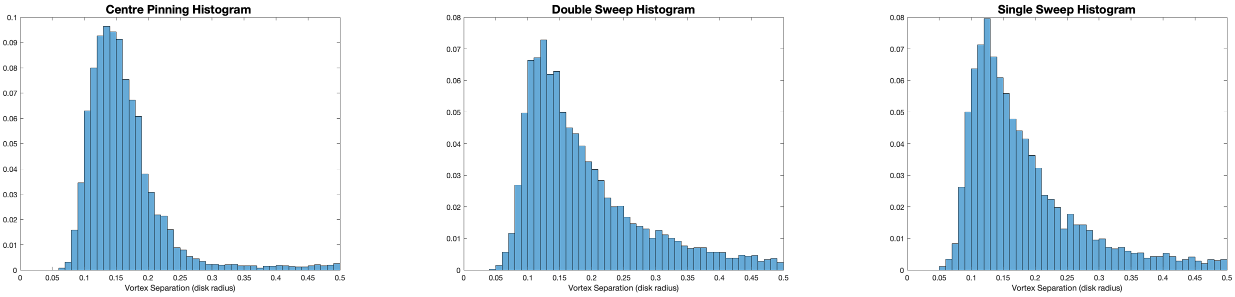

Figure 6.10: Demonstration of vortex core repulsion. In all cases the minimum nearest neighbour distance between vortices was never less than 0.05 R, corresponding to 5 μm in the experiment. This suggests enforcing a minimum vortex separation.

step, somewhat naively repositions a vortex randomly within some distance of its initial position, and only accepting changes to the energy and angular momentum that lie within the demon's tolerances. It is possible for a pair of vortices to have a low separation and very high energy, leading to the rest of the vortices being placed further apart. This leads to slightly different clustering statistics to those of the experiment and dynamic point vortex simulations. In order to crudely capture the the clustering behaviour we can just enforce a minimum vortex separation of 5 ξ, in any Monte-Carlo configuration. This leads to dipole moments that accurately match the experimental data. We are able to create histograms of the measured experimental data, and compare this to Monte-Carlo ensembles based from the average energy and angular momentum of the experimental data. This agrees well with the experimental histograms, see Fig.6.9, with the exception of the two cluster initial state. This is expected as it is a non-equilibrium state and we observe the clusters relaxation into a a single off axis-cluster in equilibrium. The dipole moment is also a measure of the clustering statistics and the experimental dipole moment of the non-equilibrium state can be seen to quickly match that of the Monte-Carlo. To further show the agreement of the Monte-Carlo simulations and experiment, that experimental vortices are in equilibrium, we time integrate the experimental vortex locations and compare this to a similarly time integrated Monte Carlo simulations, from $2s$ onwards in the experiment. While over 40 experimental runs were performed, at each timestep for each experimental initial condition, the histograms aren't very smooth, as can be seen in Fig. 6.9. Integrating the vortex locations over time result in a much comparison as can be seen in Fig. 6.12, where there very good agreement

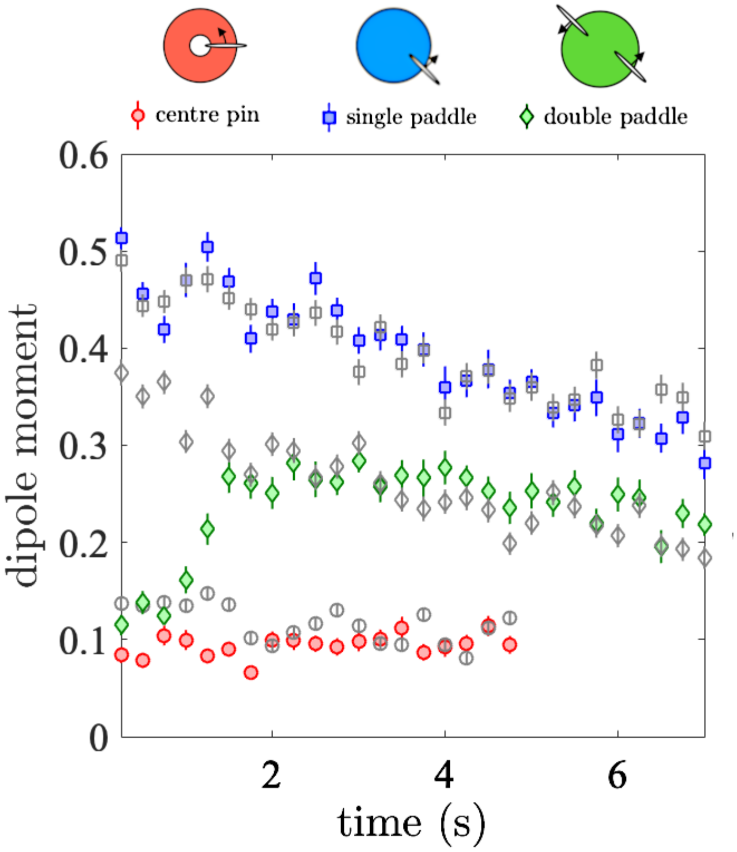

FIGURE 6.11: Demon Monte Carlo, with core repulsion, dipoles moments marked in grey. As the experimental dipole moment matches that of the demon quite closely for the single paddle sweep (off-axis cluster) and centre pin (on-axis cluster) cases, we can say that they are an equilibrium state, in agreement with the mean-field calculations performed by Smith and O'Neil presented in Chapter 3. We also see the dipole moment of the double paddle (non-equilibrium state) grows to match that of the Monte-Carlo simulation within $2s$, indicating that it has thermalised into an equilibrium state

between the experiment and simulations. This indicates that all of the three cases are in equilibrium, in good agreement with the Monte-Carlo simulation, and the mean-theory prediction presented by Smith and O'Neil [19].

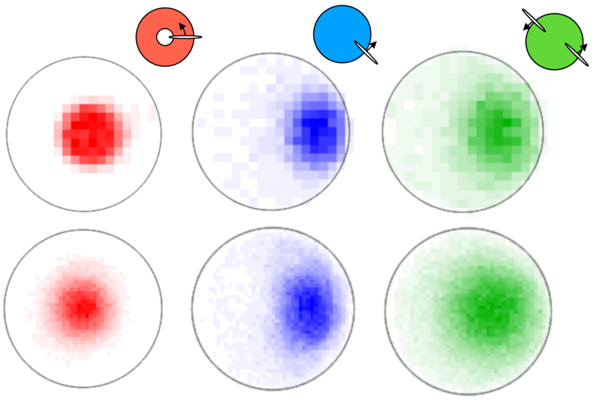

Figure 6.12: Top: time integrated experiment vortex positions, taken over a period of 4.75s, compared to by taking a individual Monte-Carlo at each time step and summing over all of them. This is as there aren't enough vortices to make smooth histograms for an individual time step. See above figure.

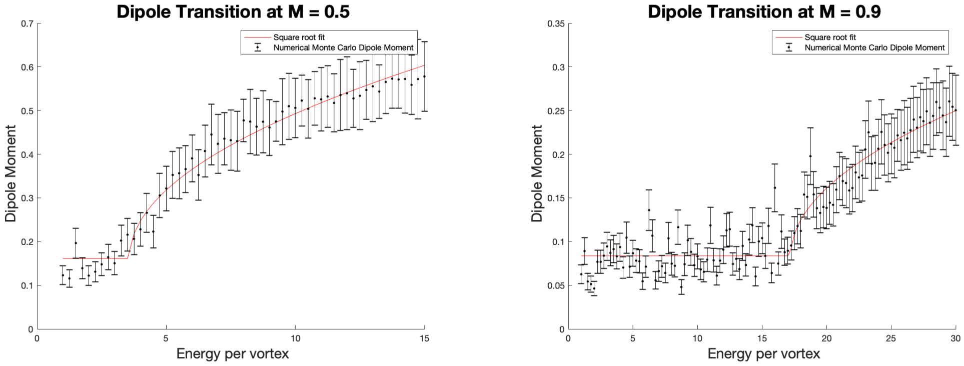

Figure 6.13: Dipole moment transition at fixed angular momentum. Note the numerical square root fit of the energy above the transition energy, where the system of the system is broken.

6.4 Symmetric breaking off-axis transition and parameter space

The defining feature of chiral system is the transition from symmetric on-axis vortex clusters to the non-symmetric off-axis vortex clusters equilibria at high energies, the primary focus of the 1990 paper by Smith and O'Neil [19]. The transition can only occur at a negative thermodynamic temperature, and resembles a second order phase transition. In order plot the parameter space, similar to Smith and O'Neil in Fig. 3.3, we calculated the dipole moment of the vortex system over a range of angular momenta and energy. At a fixed angular

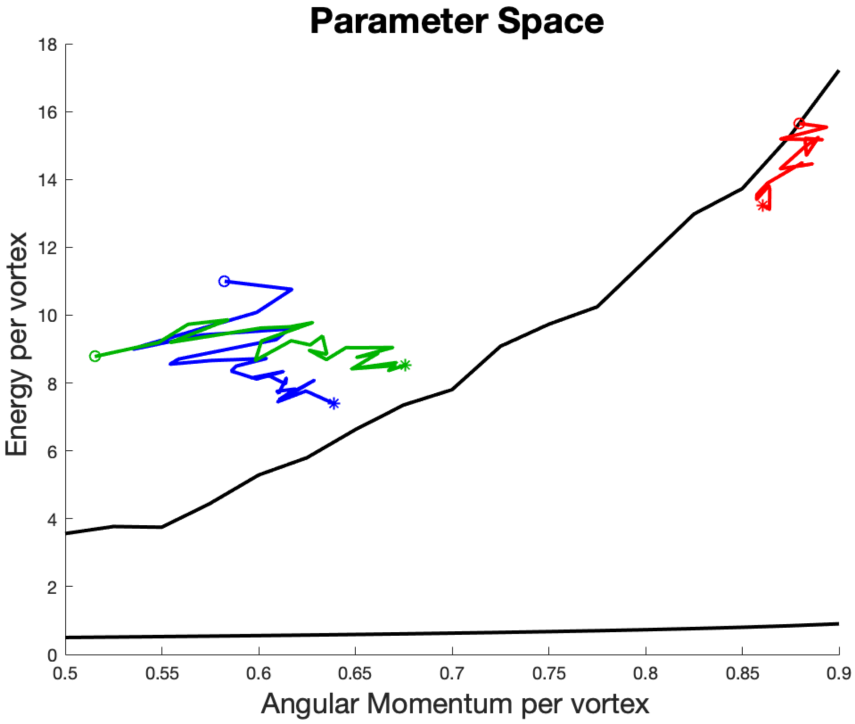

FIGURE 6.14: Plot of the parameter space. The top line separates the on-axis states from the off-axis states, while the bottom line is the minimum allowed energy given by mean-field theory $E = \frac{1}{2} - \frac{1}{4}\ln 2M$ [19]. The experimental average energy per vortex is plotted against the angular momentum per vortex, with the initial state marked with a circle and the final states marked with a star.

momentum, the dipole moment is constant below a certain energy threshold (in the infinite vortex limit the dipole moment is zero, however for a finite number of vortices this is shifted off zero). Above this energy threshold there is an approximately square root dependence of the dipole moment on energy. In order to find this transition we fit a a square function to the energy at a fixed angular momentum and record this threshold energy, see Fig. 6.13. We can then plot this and the minimum permitted energy from the mean-field theory $E_{min} = \frac{1}{2} - \frac{1}{4}\ln 2M$ [19]. It is extremely difficult to perform Monte Carlo simulations close to the minimum energy, as there are very few permitted states to sample. It should our parameter space we use $M = N_v - \sum_i r_i^2$, the condensate angular momentum, as opposed to the angular momentum that Smith and O'Neil use of $M = \sum_i r^2$. As none of the vortex cluster states that we have experimentally created have an angular momenta less than 0.5, it is unnecessary to consider them. The parameter space that we calculated, Fig. 6.14, corresponds to the upper left quadrant of that found by Smith and O'Neil, see Fig. 3.3. Interestingly Smith and O'Neil find that there is only one on-axis state when $\bar{M} = 0.5$, which corresponds to uniform distribution of vortices, however with the Monte-Carlo simulations it appears as though there are a number of allowed on-axis states at $\bar{M} = 0.5$, which is potentially a consequence of finite vortex number.

It might be informative to consider a few limiting cases. The first of which is the high energy limit, in this case all the vortices are very tightly spatially localised, almost all occupying the same point, and hence the dipole momentum $D = \bar{r}$ is simply given by $\sqrt{1-\bar{M}}$, where $\bar{M}$ is the angular momentum per vortex. The second is the low energy limit at low angular momentum. Here the vortices are distributed close to the boundary, as near the boundary the vortices are paired with their image vortices, the energy is minimised as well as the angular momentum. This results in a ring state, and as Smith and O'Neil found the on-axis states with an angular momentum less than $\bar{M} = 0.5$, with the new definition of angular momentum, are all ring states.

We have found excellent agreement between experimental data and the point vortex model. We also found that while GPE simulations accurately capture vortex nucleation they do not accurately capture the off-axis transitions and more sophisticated simulations are necessary. We have found that the dynamics of the vortices are accurately captured by a dynamic point vortex equation with a stochastic term. Monte-Carlo simulations show that the vortices are in, or very close to, a thermal equilibrium at every time apart the double paddle sweep which thermalises after approximately 2 s. This is a very interesting toy system that we have a great deal of control over.

7

Dynamics of Vortex Dipoles and an analogy to Snell's Law

As discussed in Chapter 4, Cawte et al. [29], derive an analogous Snell's law relation for dipoles across a step change in density in a BEC. They verify this relation by direct comparison to a GPE simulation, and find excellent agreement. Our goal was to experimentally implement, and observe the dipole trajectories directly. Previous work by Gauthier [13, 32] indicate that creating a step change in condensate density is achievable using the technique of half-toning, possibly refined using the feedforward technique, discussed in Section 5.2.2. While our GPE simulations, for a realistic experimental scheme, agree excellently with the results of Cawte et al. it appears as though the step changes made through the use of half-toning don't create smooth condensates for the dipoles. The Snell's law behaviour can be still be observed in a condensate of linearly varying density, analogous to the trajectory of a photon in a fibre-optic cable or a shock wave through the atmosphere. Due an experimental fault, the condensate number may have varied dramatically from shot to shot, however qualitatively, dipole trajectories match that of GPE simulations. At the time of publication of this thesis, the experiment is operational and will hopefully conducted soon. The experiment could be extended to deterministically create Jones-Roberts solitons [53], create "optics" to manipulate vortex dipoles, probe equilibrium vortex states of the condensate, and observe soliton vortex interactions.

7.1 GPE simulations

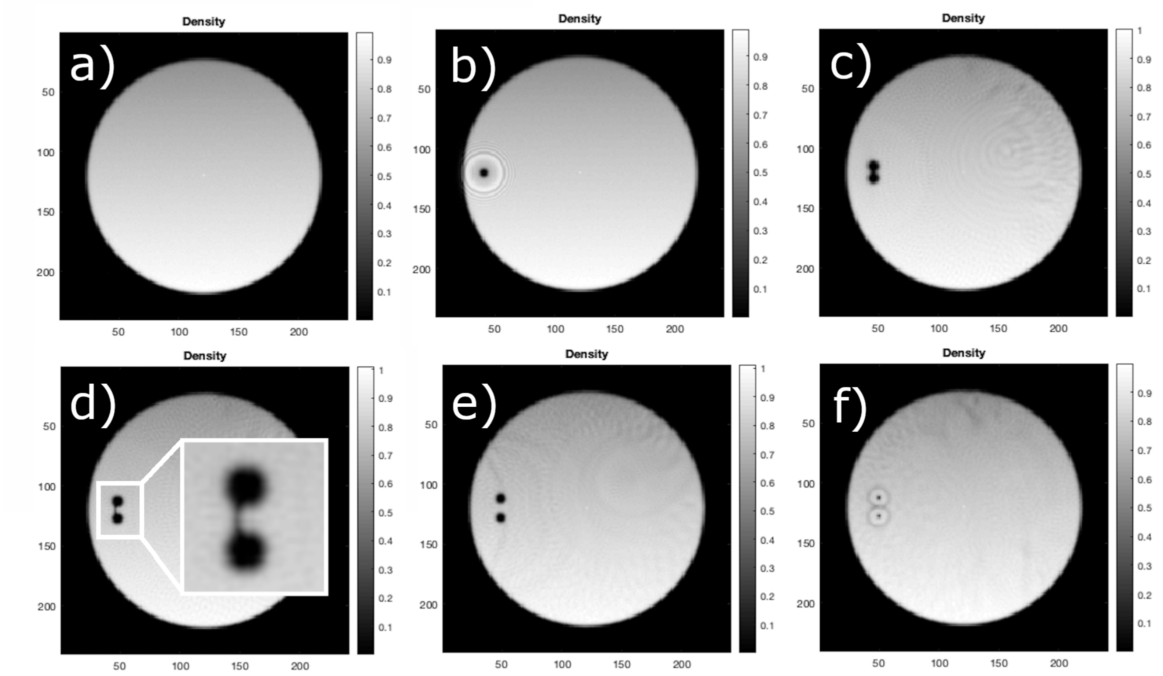

FIGURE 7.1: "chopsticks" nucleation method, with images shown at 0τ,b) 60τ, c) 300τ, d) 320τ, e) 400τ, and f) 540τ. d) has an in-figure of the short-lived grey soliton state, potentially of interest to future studies.

In order to create a simulation of an experimentally implementable sequence, we use a 100ξ circular confining potential, with an additional step potential of either 0.1, 0.2, or 0.3μ, to create a step in condensate density. Dipoles were nucleated using the "chopsticks" method at 33 different angles to the interface ranging from $\theta = 0$ to $\theta = \pi/2$, the trajectories of the centre of the dipoles are shown in Fig. 7.3 along with the agreement between the dipole positions and Snell's law. The outgoing angles from interaction with the interface agree excellently with both Snell's law or reflection, see Fig 7.2 for example trajectories with reflection and refraction. There are a few dipole trajectories in the anomalous capture regime described by Cawte et al. These travel along the interface and interact with image vortices before either clear reflection or refraction, an unfortunate consequence of the finite condensate size permitted by the experiment. Experimentally it seems likely that the anomalous capture regime could be explored in any detail due to noise and inhomogeneities in the system. While performing the dipole nucleation with "chopsticks", see Fig. **??**, we observe a temporary grey soliton as the condensate phase relaxes to a change of 2π. While it was noted that the phase relaxes when producing dipole pairs by Samson et al. [54], and that a dark soliton could be created for a π jump, they make no note of the creation of grey solitons. This could potentiality be exploited in future experiments.

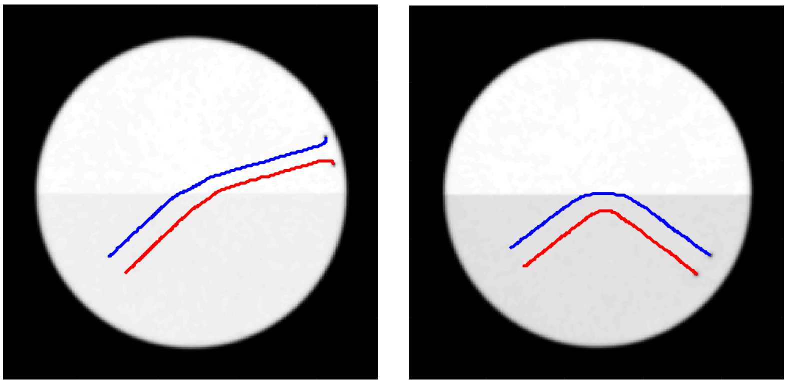

FIGURE 7.2: Example GPE simulations of dipole trajectories. Left, refraction with $\rho_1/\rho_2 = 0.95$, $\theta = 46°$. Right, reflection with $\rho_1/\rho_2 = 0.89$, $\theta = 52°$, the red is the trajectory of the vortex and the blue line gives the trajectory of the anti-vortex. The vortices are travelling left to right

7.2 Experimental dipole optics

Similar to the previous experiment, condensates of around 4×10^6 atoms were formed in the red detuned (1064 nm) highly oblate sheet with a trapping frequency of $(\omega_x, \omega_y, \omega_z) = 2\pi(1.8, 1.6, 106)$. Extra trapping in the x-y plane was applied with blue detuned (532 nm) laser light reflected from the DMD with a trap depth of around 5μ. The DMD trap was used

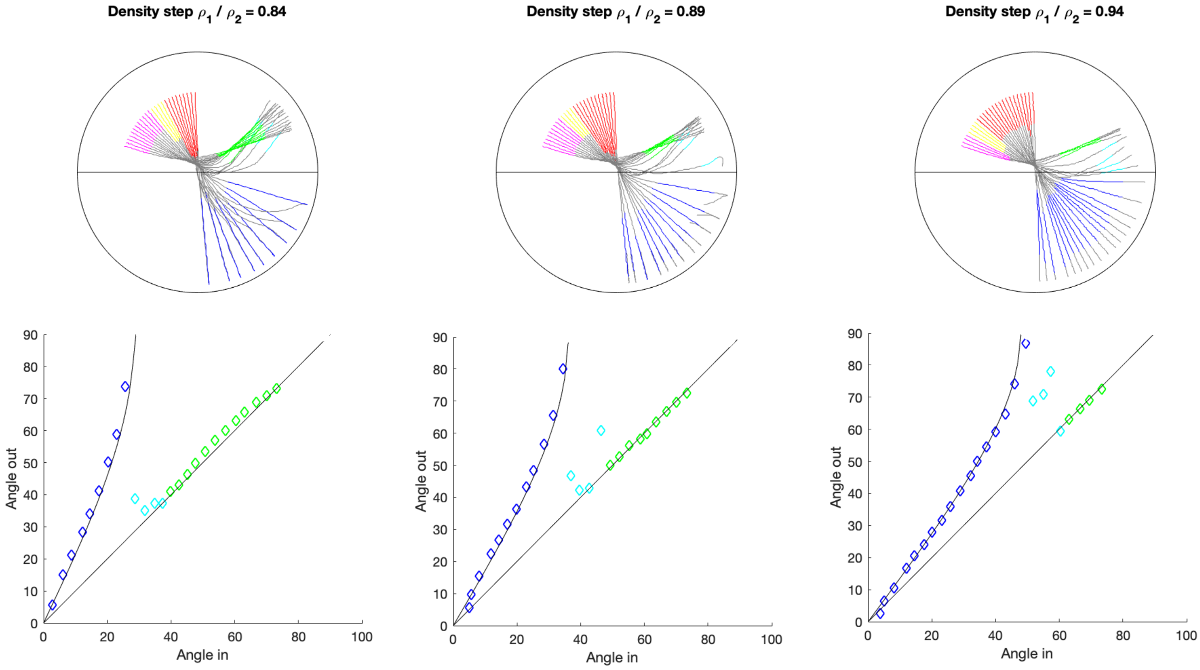

Figure 7.3: Left to right, step potentials with a difference of $\rho_1/\rho_2 = 0.84$, 0.89 and 0.94 respectively. Top: trajectories of the average vortex position from GPE simulations in grey. The initial linear trajectories of the vortices are marked in red, yellow, and purple for the refractive, anomalous capture, and reflective regimes respectively. Note that the trajectories of dipoles in the anomalous capture regime interact with their images before the outgoing angles can be accurately measured. Bottom: relation of the ingoing dipole angle to the outgoing dipole angle. We see that this obeys Snell's law in dark blue, and the law of reflection, in green. The regime of anomalous capture is presented in light blue

to create a circular trap with a diameter of $100\mu m$. This is nearly a hardwall potential, due to the PSF with a radius of $610nm$. The resulting condensate in this potential was relatively homogeneous. The condensate has a healing length of around $\xi = 500nm$, in the centre of the trap, and a Thomas-Fermi diameter of $6\mu m$ vertically, resulting in a Bogoliuabov speed of sound of $1290\mu m/s$. Care was also taken to ensure that magnetic fields across the condensate were controlled with the side zeroing coils, and either cancelled, or a applying a linear gradient. As the vortex size is on the order of the healing length around the resolution limit of the imaging system, a brief 5 ms TOF was used to expand the vortex core size.

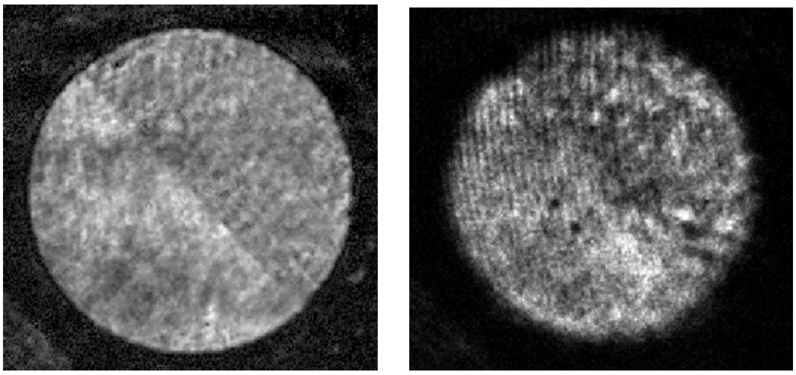

Figure 7.4: Experimental implementation of half-toning and chopsticks: top image, in-situ imaging of the BEC after using feedback, notice the quite smooth potentials. Bottom, imaging vortices created with the chopsticks technique with $5ms$ time of flight.

7.2.1 Hard interface

Dipoles created in the halftoned potential were consistent in their nucleation and initial position. Unfortunately, despite much experimentation with initial parameters and with the feedforward technqiue described in Section. 5.2.2, it appears as though vortex dipoles do not travel in straight lines in a half-toned potentials, as the dipole position vary immensely at the same hold time. The reasons for this are unclear, however it may be due to minute density fluctuations, on the order of the healing length. This would effectively perturb the vortices, making their motions stochastic [1]. While it may be possible to create a smooth potential using some mix of half-toning, feedback, it was decided to attempt to see Snell's law behaviour in a continuous linearly varying density, analogous to a continual changing refractive index.

7.2.2 Linearly varying density

Using the side zeroing coils around the science cell, typically used to cancel stray magnetic fields, we can shift the zero of the confining quadruple trap. This effectively adds a linearly changing magnetic field across the condensate, and as the atoms at in the $|F = 1, m_F = -1\rangle$ magnetically trappable state, they are subjected to a linear potential. The motion of dipoles through this changing background density is analogous to curved trajectories of photons in a fibre optic cable. As expected the vortex paths are no longer straight, and due to changing background density the separation of the dipole pair changes over the trajectory. We observe the formation of Jones-Roberts solitons, and the separation between the vortices increasing to the degree that their dynamics are dominated by their image vortices, under certain conditions.

---

[1] In other experiments I have conducted, it appears as though half-toning can create bulk density waves and can be used to induce excited azimuthal modes of a confining geometries reliably suggesting half-toning is effective on the order of $10\mu m$

GPE simulations

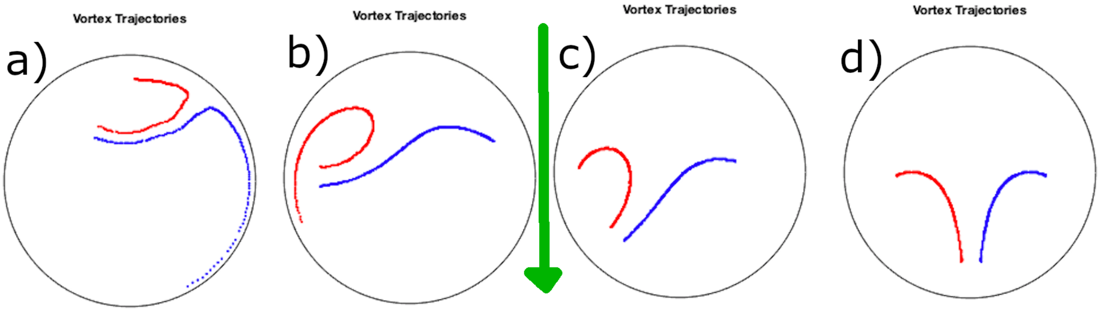

FIGURE 7.5: Tracked Vortex Trajectories from a GPE simulation for the initial conditions a) 45° b) 90° c) 135° and d) 180°, with the direction of the applied magnetic field indicated with the green arrow. Vortices travelling towards the arrow are travelling into a region of lower condensate density. A more detailed picture of case b) is shown in Fig. 7.6

GPE simulations of the this system is almost identical to that of the step potential system, but a linearly changing external potential is applied, rather than the step. The initial angle of the chopsticks are changed as before and dipoles are released to freely evolve. In these simulations changing the gradient of the linearly applied potential corresponds to changing the strength of the magnetic field applied from the side zeroing coils. This means the strength of the magnetic field, or linear potential, and the initial dipole position and separation completely characterise the trajectories. While the magnetic field strength of the simulations was not matched to the experiment, to find the qualitative behaviour of the system, I applied a seemingly reasonable linear potential resulting in curved dipole trajectories.

Two interesting cases involve the dipoles being released at an angle of $\theta = 0°$ or $\theta = 180°$

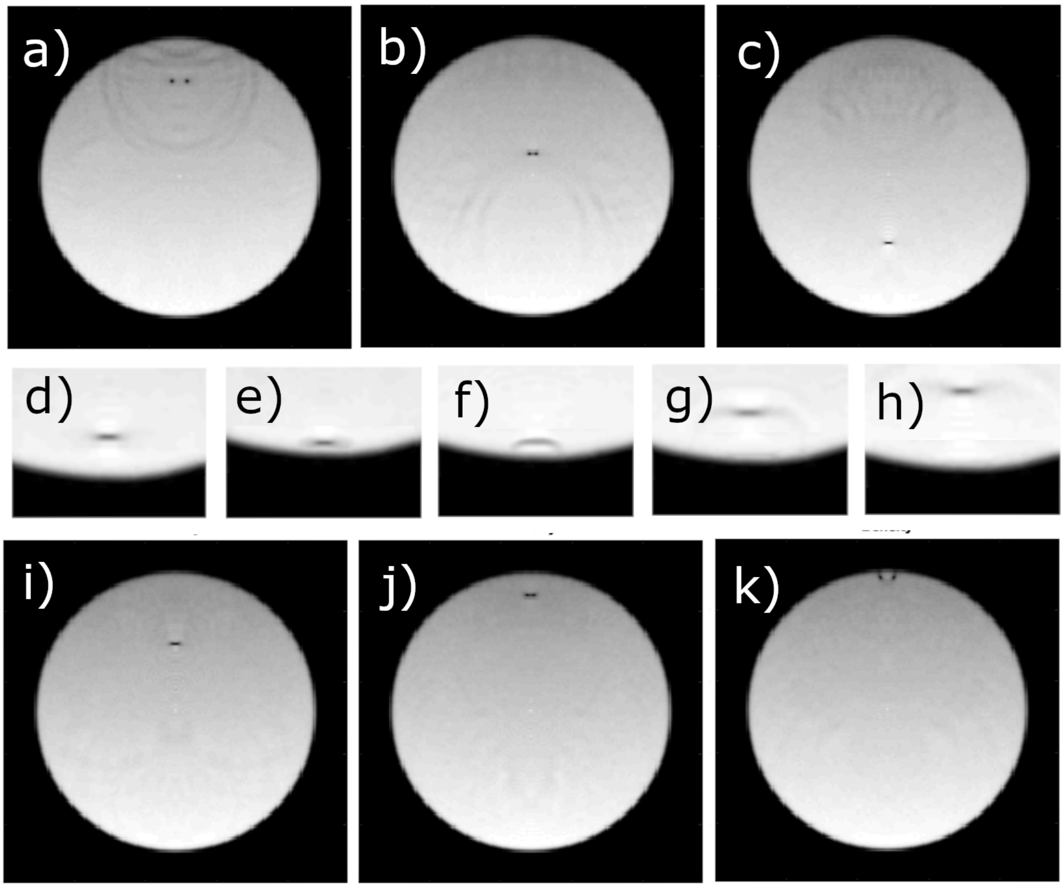

Figure 7.6: Dipole trajectory travelling towards a high condensate density $\theta = 0°$. Top a) 1000τ, b) 1340τ, c) 1500τ Middle: d) 1560τ, e) 1570τ, f) 1580τ, g) 1590τ, h) 1600τ. Bottom: i) 1800τ, j) 1900τ, k) 1970τ. We first observe the dipole that condenses into a Jones-Roberts soliton (JRS) a)-c). The JRS then reflects off the boundary d)-h), then re separates into a dipole pair in the low density area of the condensate i)-k). The nature of the dipoles can clearly can seen at the boundary, where the vortices pair up with their images, while the JRS reflects. This is a definitive indication of a JRS, and may be observable experimentally.

to the linear gradient. In the first case, with $\theta = 0$, the dipole is moving from an area of low background density to high background density, this means the vortices can merge into Jones-Roberts soliton (JRS), where the topological defects of the vortices annihilate, create a π phase jump over a soliton. This then travels at the Bogoliuabov speed of sound, and reflects off the boundary, a completely different behaviour to a dipole, which when approaching a hardwall will separate and the vortices will pair up with their images. The reflected Jones-Roberts soliton then travels from an area of high density and low density and separates back into a vortex anti-vortex pair, which separate as they pair with their images at

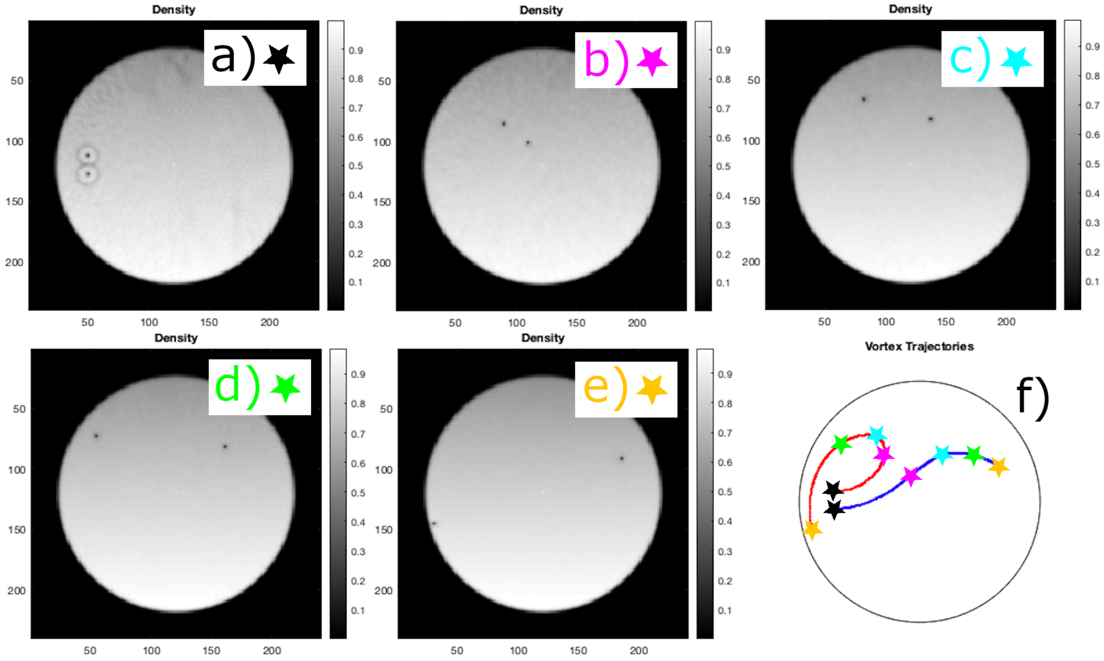

FIGURE 7.7: Example vortex positions for the initial dipole angle $\theta_i = 90°$ various time steps 540τ,1640τ,2740τ, 3840τ, 4940τ for the case with marked vortex positions on the vortex trajectories. Notice the curved vortex dipole trajectory, in stark contrast to the previous examples of straight vortex trajectories.

the boundary. For a dipole travelling in the opposite direction $\theta = 180$, from high density to low density, the verticex separation must grow. As the vortices move further apart their interaction with their image vortices begins to dominate and they curve back around forming a closed orbit. These simulations have a high degree of symmetry and little noise, it is unlikely to observe these exact behaviours for vortices and JRS in an experiment.

Initial angles other than $\theta = 0°$ or $180°$, have curved trajectories. Dipole initially in low condensate densities have a relatively constant separation and curve toward the area of low density. Similarly the vortices are released at a $\theta = 90$ angle to the linear gradient, curve towards the area of low density, however the vortex separation quickly grows. For dipoles starting in the high density region, the dipole separation becomes significant quickly and their interaction becomes negligible in comparison to the image vortex effects.

Preliminary Experimental Data

During the collection of this data there as an intermittent fault where condensates would not consistently load, and condensate number would vary significantly shot to shot. At the time no cause could be identified, however, the BEC transfer coil failed a couple of weeks later. It seems unusual for a coil to intermittently fail, however it would explain the behaviour of the experiment[2]. As such the condensate density from shot to shot could vary significantly, changing the healing length and hence dimensions of the required simulation. Experimentally this would imply that both the trajectories can vary shot to shot as well as the speed of the dipole. Due to this limitation this data is only preliminary and a quantitative comparison between the data and numerical models is not attempted with only a qualitative comparison. However, we do observe qualitative agreement between experimental data and the GPE simulations.

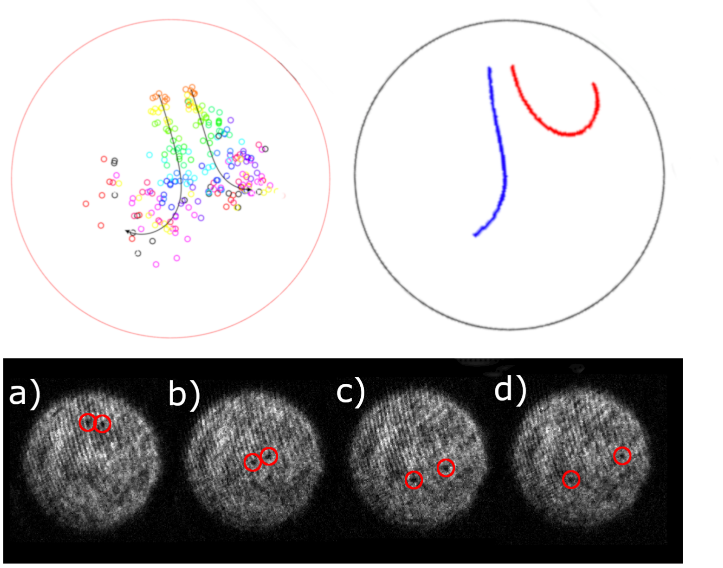

Figure 7.8: Dipole initial created at angle $\theta = 180$. Top left, marked vortex positions from the experiment with a drawn arrow indicating vortex direction. The marker colour indicates the vortex observation time. Top right, a similar GPE simulation to provide a comparison. Bottom images taken at a) $0s$, b) $100ms$, c) $200ms$, and d) $300ms$.Images taken at a) $0s$, b) $100ms$, c) $200ms$, and d) $300ms$.

---

[2] This failure was somewhat expected as the coils are immersed in water to cool them. The coils corrode and must be replaced periodically. They fail due to the high stress placed on them from the high magnetic fields, and deform in shape.

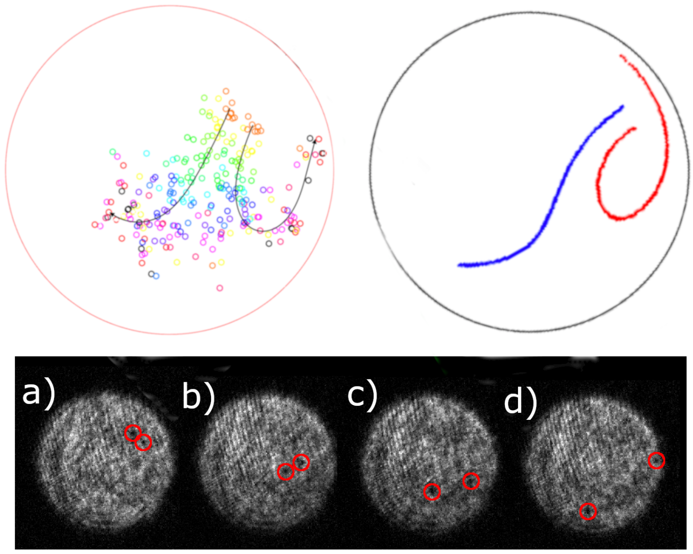

FIGURE 7.9: Dipole initial created at angle $\theta = 225$. Top left, marked vortex positions from the experiment with a drawn arrow indicating vortex direction. The marker colour indicates the vortex observation time. Top right, a similar GPE simulation to provide a comparison. Bottom images taken at a) $0s$, b) $100ms$, c) $200ms$, and d) $300ms$.

Preliminary experimental data is presented in Fig. 7.8 and Fig. 7.9, next to example dipole trajectories found with a GPE simulation. While this qualitatively matches the vortex trajectories, future experimental data with hopefully permit a direct comparison with simulations. It should also be possible to create a inhomogeneous point vortex model for this system, thereby expanding our knowledge of point vortex physics.

8

Conclusion

8.1 Summary

The UQ BEC apparatus is ideal for performing experiments on a two dimensional superfluids. In particular Gauthier and Neely [13, 13, 32] have demonstrated the versatility of this apparatus, using the digital micromirror device (DMD), to create almost arbitrary dynamic potentials, providing a high degree of control over the condensate.

We first investigate a system of single signed vortices, the chiral system, which are well described by the point vortex model. Lars Onsager used the point vortex model to predict vortex clustering at high energies, described by negative thermodynamic temperatures [12]. Furthermore this system has symmetric and asymmetric equilibrium states, with a symmetry breaking transition that can only occur at negative temperatures, a result previously found by Smith and O'Neil [19]. We have experimentally created these symmetric and asymmetric states as well as a non-equilibrium initial state. We have observed both the stability of the the equilibrium states as well as the relaxation of a non-equilibrium state into a asymmetric state. Using a variety of modelling techniques we observe that the nucleation and dynamics of the vortices are qualitatively well described by the Gross-Pitaevskii equation. We also observe excellent agreement between the data, a dynamic point vortex model, and with a Monte-Carlo point vortex simulation. This shows demonstrates vortices in the experiment are in an equilibrium. Whilst the vortices are in equilibrium they form a subsystem of the condensate which is highly non-equilibrium. The results presented in this thesis, agree with Smith and O'Neil, with minor differences owing the the finite vortex number.

Secondly we also use a method pioneered by Samson et al [54], to create on-demand pairs of vortices and anti-vortices. This is a highly versatile method that we use to explore the motion of vortex dipoles in an inhomogeneous condensate. Due to the conservation of energy and linear momentum of the vortices, the dipoles should obey a Snell's law relation with reflection and refraction across a step change in condensate density [29]. We simulate an experimentally realistic scheme using "chopsticks" and find excellent agreement with Snell's law. Due to experimental limitations, we instead investigate the behaviour of dipoles in condensate with linearly varying density. Preliminary experimental data qualitatively agrees well with GPE simulations.

8.2 Outlook

While we understand much of the behaviour of the chiral system, there remain some open questions. It is not known why the Brownian motion term in the point vortex model leads to such good agreement with the experimental data. Potentially a projected or stochastic projected GPE simulation would provide insight. We could perform many simulations using imprinted initial vortices, matching experimental data. We are yet to make comparisons to mean-field theory, a semi-analytic theory that should in principle completely characterise the system in the large vortex limit. This comparison would be interesting due to finite number of vortices in the experiment. We have not experimentally explored the behaviour of the vortex ring states that Smith and O'Neil discuss, which would completely characterise the parameter space.

As of the time of submitting this thesis, the experiment is operational. The dipole Snell's law experiments should be performed soon. Depending on the quality of data, quantitative comparisons to GPE and an inhomogeneous point vortex model could be made. Using the varying condensate density, it should also be possible to create on-demand Jones-Roberts solitons, and potentially create "sound lenses". More generally, using the versatility of the chopsticks dipole creation process, it should be possible to create stable initial vortex configurations, such as a steady two vortex state and vortex lattices, and explore the onset of chaos experimentally. It is also possible to explore the dynamics of soliton-soliton, soliton-dipole, and dipole-dipole interactions. The content of this thesis demonstrates the potential for conducting a wide range of vortex experiments, with good agreement to theory. The experiment is a playground for the exploration of vortex physics.

A

Computational solving the GPE

XMDS2

XMDS2 is a fast general differential equation initial value problem solver that can be used to numerically solve coupled, partial and stochastic in arbitrary dimensions [67]. XMDS2 allows a problem to be expressed in XML format and automatically outputs a C++ simulation written with fast algorithms that can be parallelised. It is used in a wide range of fields from quantum many-body systems to ecology. Other programs and numerical techniques could have been utilised such as writing a custom simulation in C using the Crank-Nicolson method. However a numerical problem can be specified in XMDS2 in high level XML and XMDS2 will output a simulation written in low level optimised C++ code, thus saving a significant amount of time writing and debugging code while providing a high degree of flexibility. This was ideal for simulating the BEC using a unitless 2D GPE.

Unitless two dimensional GPE

In order to reduce computational complexity it is useful to perform simulations in unitless dimensions. Here we choose spatial units in terms of the healing length, and temporal units in terms of the healing time. It is also often quite convenient to work in a frame that is evolving in phase with the rate of the chemical potential by subtracting the chemical potential from the potential. The presence or absence of the chemical potential in that expression has no effect on the dynamics and can be included or neglected as a matter of choice.

$$i\hbar\partial_t\Psi(\mathbf{r},t) = \left[-\frac{\hbar^2}{2m}\nabla^2 + V_{ext}(\mathbf{r},t) + g|\Psi(\mathbf{r},t)|^2\right]\Psi(\mathbf{r},t) \tag{A.1}$$

Making the substitutions $\mathbf{r}' = \mathbf{r}/\epsilon$ and $t' = t/\tau$ with $\xi^2 = \hbar^2/mng$ and $\tau = m\xi^2/\hbar = \hbar/ng$ we get

$$i\hbar\frac{1}{\tau}\partial_{t'}\Psi(\mathbf{r}',t') = \left[-\frac{\hbar^2}{2m}\frac{1}{\xi^2}\nabla'^2 + V_{ext}(\mathbf{r}',t') + g|\Psi(\mathbf{r}',t')|^2\right]\Psi(\mathbf{r}',t') \tag{A.2}$$

$$i\hbar\frac{ng}{\hbar}\partial_{t'}\Psi(\mathbf{r}',t') = \left[-\frac{\hbar^2}{2m}\frac{mng}{\hbar^2}\nabla'^2 + V_{ext}(\mathbf{r}',t') + g|\Psi(\mathbf{r}',t')|^2\right]\Psi(\mathbf{r}',t') \tag{A.3}$$

Now simplifying and dividing by a factor ng

$$i\partial_{t'}\Psi(\mathbf{r}',t') = \left[-\frac{1}{2}\nabla'^2 + \frac{V_{ext}(\mathbf{r}',t')}{ng} + |\Psi(\mathbf{r}',t')|^2/n\right]\Psi(\mathbf{r}',t') \tag{A.4}$$

Now normalising the wavefunction by $\Psi = \phi/\sqrt{n}$ and dividing both sides by $\sqrt{n}$ we get

$$i\partial_{t'}\phi(\mathbf{r}',t') = \left[-\frac{1}{2}\nabla'^2 + V'_{ext}(\mathbf{r}',t') + |\phi(\mathbf{r}',t')|^2\right]\phi(\mathbf{r}',t') \tag{A.5}$$

Where I have re-expressed the potential in units of the chemical potential $V'_{ext}(\mathbf{r}',t') = V_{ext}(\mathbf{r}',t')/ng$. Now assuming that the wavefunction vertical is strongly trapped in a harmonic potential, we can assume it is in the Thomas-Fermi groundstate vertically $\phi(\mathbf{r}',t') = \psi(\mathbf{x}',t')\phi(z')$

$$i\partial_{t'}\psi(\mathbf{x}',t')\phi(z') = \left[-\frac{1}{2}\nabla'^2 + V'_{ext}(\mathbf{r}',t') + |\psi(\mathbf{x}',t')\phi(z')|^2\right]\psi(\mathbf{x}',t')\phi(z') \tag{A.6}$$

Now left multiplying both sides by $\phi(z')^{-1}$ and integrating over $\int \mathrm{d}z'\, |\phi(z')|^2 = 1$, we end up with

$$i\partial_{t'}\psi(\mathbf{x}',t') = \left[-\frac{1}{2}\nabla'^2 + V'_{ext}(\mathbf{r}',t') + |\psi(\mathbf{x}',t')|^2\right]\psi(\mathbf{x}',t') \tag{A.7}$$

$$\partial_{t'}\psi(\mathbf{x}',t') = i\left[\frac{1}{2}\nabla'^2 - V'_{ext}(\mathbf{r}',t') - |\psi(\mathbf{x}',t')|^2\right]\psi(\mathbf{x}',t') \tag{A.8}$$

Finally in order to model phenomological damping effects we add a γ_0 term to capture effects such as interactions with the thermal cloud

$$\partial_{t'}\psi(\mathbf{x}',t') = (i+\gamma_0)\left[\frac{1}{2}\nabla'^2 - V'_{ext}(\mathbf{r}',t') - |\psi(\mathbf{x}',t')|^2\right]\psi(\mathbf{x}',t') \tag{A.9}$$

$$\tag{A.10}$$

XMDS2 utilises pseudo-spectral methods. This can cause problems when momenta in the simulation are higher than the maximum momenta imposed by the finite lattice spacing $k_{max} = 1/2a$ where a is the grid spacing. This requires finer grid spacings for some simulations. For the later "chopsticks" simulations only a (240×240) grid is required; however, for the"paddle sweep" simulations to nucleate vortex clusters, higher momenta modes are excited due to the relatively thin paddle widths and required grid sizes of (400×400). Almost hardwalled potentials are used with some smoothing to reduce computational time and better simulate the experiment.

Detecting the vortex positions in simulations

It is possible to numerically detect the positions of point vortices and their sign by taking the curl of the velocity. This is only non-zero when a vortex is present.

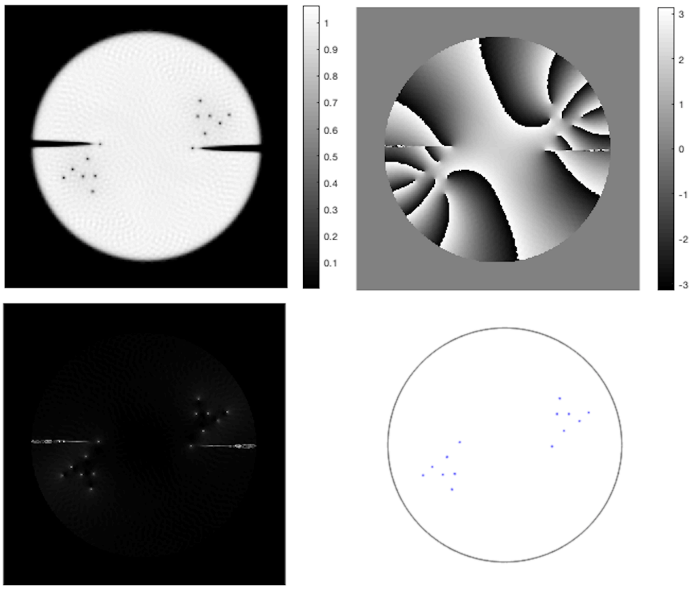

FIGURE A.1: As the simulation outputs the phase and density of the wavefunction, it is possible to numerically locate vortex positions by taking the curl of the velocity field $\nabla \times \nabla\phi$. In our unitless simulation this should evaluate to ±1 at vortex cores and 0 elsewhere. In order to account for regions with very sparse density I have applied a mask, this requires a that the circulation is around 1 and a local minimum.

References

[1] T. Meuel, Y. L. Xiong, P. Fischer, C. H. Bruneau, M. Bessafi, and H. Kellay. *Intensity of vortices: from soap bubbles to hurricanes.* Scientific Reports **3**(1) (2013).

[2] Ljenner. *Oma (southern pacific ocean)* (2019).

[3] T. Greicius. *Juno image gallery* (2015).

[4] M. H. Anderson, J. R. Ensher, M. R. Matthews, C. E. Wieman, and E. A. Cornell. *Observation of bose-einstein condensation in a dilute atomic vapor.* Science **269**(5221), 198 (1995).

[5] *The kolmogorov 1941 theory.* Turbulence pp. 72–99.

[6] A. Tsinober. *An Informal Introduction to Turbulence* (Springer Netherlands, 2004).

[7] C. E. Leith and R. H. Kraichnan. *Predictability of turbulent flows.* Journal of the Atmospheric Sciences **29**(6), 1041 (1972).

[8] H. Aref, P. L. Boyland, M. A. Stremler, and D. L. Vainchtein. *Turbulent statistical dynamics of a system of point vortices.* Fundamental Problematic Issues in Turbulence pp. 151–161 (1999).

[9] T. Tatsumi. *Turbulence and chaotic phenomena in fluids: proceedings of the international symposium, Kyoto, 5-10 September, 1983* (North-Holland, 1984).

[10] J. V. Neumann. *Recent theories of turbulence* (Collected works, vol. 6, pp. 439,441,448, 462, ed. A.H. Taub, Pergamon, 1950).

[11] P. Tabeling. *Two-dimensional turbulence: a physicist approach.* Physics Reports **362**(1), 1 (2002).

[12] L. Onsager. *Statistical hydrodynamics.* Il Nuovo Cimento **6**(S2), 279 (1949).

[13] G. Gauthier, M. T. Reeves, X. Yu, A. S. Bradley, M. Baker, T. A. Bell, H. Rubinsztein-Dunlop, M. J. Davis, and T. W. Neely. *Negative-temperature onsager vortex clusters in a quantum fluid.* arXiv preprint arXiv:1801.06951 (2018).

[14] S. P. Johnstone, A. J. Groszek, P. T. Starkey, C. J. Billington, T. P. Simula, and K. Helmerson. *Order from chaos: Observation of large-scale flow from turbulence in a two-dimensional superfluid.* arXiv preprint arXiv:1801.06952 (2018).

[15] H. Helmholtz. *ber integrale der hydrodynamischen gleichungen, welche den wirbelbewegungen entsprechen.* J. Reine Angew. Math. **55**, 25 (1858).

[16] H. Aref. *Point vortex dynamics: A classical mathematics playground.* Journal of Mathematical Physics **48**(6), 065401 (2007).

[17] J. Barra and F. Bouchet. *Statistical mechanics and long range interactions.* Comptes Rendus Physique **7**(3-4), 414 (2006).

[18] T. Dauxois. *Dynamics and thermodynamics of systems with long range interactions* (Springer, 2002).

[19] R. A. Smith and T. M. O'Neil. *Nonaxisymmetric thermal equilibria of a cylindrically bounded guiding center plasma or discrete vortex system.* Physics of Fluids B: Plasma Physics **2**(12), 2961 (1990).

[20] G. L. Eyink and K. R. Sreenivasan. *Onsager and the theory of hydrodynamic turbulence.* Reviews of Modern Physics **78**(1), 87 (2006).

[21] P. B. Rhines. *Waves and turbulence on a beta-plane.* Journal of Fluid Mechanics **69**(03), 417 (1975).

[22] A. Venaille and F. Bouchet. *Oceanic rings and jets as statistical equilibrium states.* Journal of Physical Oceanography **41**(10), 1860 (2011).

[23] Miller, Weichman, and Cross. *Statistical mechanics, euler's equation, and jupiter's red spot.* Physical review. A, Atomic, molecular, and optical physics **45**(4), 2328 (1992).

[24] P. H. Chavanis. *From jupiter's great red spot to the structure of galaxies: Statistical mechanics of two dimensional vortices and stellar systems.* Annals of the New York Academy of Sciences **867**(1), 120 (1998).

[25] P.-H. Chavanis. *Statistical mechanics of two-dimensional vortices and stellar systems.* Dynamics and Thermodynamics of Systems with Long-Range Interactions Lecture Notes in Physics pp. 208–289 (2002).

[26] P.-H. Chavanis. *Kinetic theory of stellar systems, two-dimensional vortices and hmf model.* Theoretical and Computational Fluid Dynamics **24**(1-4), 217 (2009).

[27] A. Griffin, D. W. Snoke, and S. Stringari. *Bose-Einstein condensation* (Cambridge Univ. Press, 2002).

[28] C. Pethick and H. Smith. *Bose-Einstein condensation in dilute gases* (Cambridge University Press, 2008).

[29] M. M. Cawte, X. Yu, B. P. Anderson, and A. S. Bradley. *Snell's law for a vortex dipole in a bose-einstein condensate.* arXiv preprint arXiv:1811.02110 (2018).

[30] P. K. Newton. *The N- vortex problem: analytical techniques* (Springer, 2011).

[31] N. McKay Parry. *Design, construction, and performance towards a versatile 87rb and 41k bec apparatus* (2016).

[32] G. Gauthier. *Transport and turbulence in quasi-uniform and versatile bose-einstein condensates* (2019).

[33] K. B. Davis, M. O. Mewes, M. R. Andrews, N. J. van Druten, D. S. Durfee, D. M. Kurn, and W. Ketterle. *Bose-einstein condensation in a gas of sodium atoms.* Phys. Rev. Lett. **75**, 3969 (1995).

[34] E. P. Gross. *Structure of a quantized vortex in boson systems.* Il Nuovo Cimento **20**(3), 454 (1961).

[35] L. Pitaevskii. *Vortex lines in an imperfect bose gas.* Sov. Phys. JETP **13**(2), 451 (1961).

[36] E. J. Yarmchuk, M. J. V. Gordon, and R. E. Packard. *Observation of stationary vortex arrays in rotating superfluid helium.* Physical Review Letters **43**(3), 214 (1979).

[37] H. F. Hess, R. B. Robinson, R. C. Dynes, J. M. Valles, and J. V. Waszczak. *Scanning-tunneling-microscope observation of the abrikosov flux lattice and the density of states near and inside a fluxoid.* Scanning Tunneling Microscopy Perspectives in Condensed Matter Physics pp. 238–240 (1993).

[38] P. Engels, I. Coddington, V. Schweikhard, and E. A. Cornell. *Vortex lattice dynamics in a dilute gas bec.* Journal of Low Temperature Physics **134**(1/2), 683 (2004).

[39] R. P. Feynman. *Superfluidity and superconductivity.* Reviews of Modern Physics **29**(2), 205 (1957).

[40] Y. Kimura. *Motion of two point vortices in a circular domain.* Journal of the Physical Society of Japan **57**(5), 1641 (1988).

[41] A. J. Groszek, D. M. Paganin, K. Helmerson, and T. P. Simula. *Motion of vortices in inhomogeneous bose-einstein condensates.* Physical Review A **97**(2), 023617 (2018).

[42] H. M. Nilsen, G. Baym, and C. J. Pethick. *Velocity of vortices in inhomogeneous bose-einstein condensates.* Proceedings of the National Academy of Sciences **103**(21), 7978 (2006).

[43] D. M. Jezek and H. M. Cataldo. *Vortex velocity field in inhomogeneous media: A numerical study in bose-einstein condensates.* Physical Review A **77**(4) (2008).

[44] F. E. A. D. Santos. *Hydrodynamics of vortices in bose-einstein condensates: A defect-gauge field approach.* Physical Review A **94**(6) (2016).

[45] G. Joyce and D. Montgomery. *Negative temperature states for the two-dimensional guiding-centre plasma.* (1972).

[46] B. Mcdonald. *Numerical calculation of nonunique solutions of a two-dimensional sinh-poisson equation.* Journal of Computational Physics **16**(4), 360 (1974).

[47] D. L. Book, S. Fisher, and B. E. Mcdonald. *Steady-state distributions of interacting discrete vortices.* Physical Review Letters **34**(1), 4 (1975).

[48] X. Yu, T. P. Billam, J. Nian, M. T. Reeves, and A. S. Bradley. *Theory of the vortex-clustering transition in a confined two-dimensional quantum fluid.* Physical Review A **94**(2) (2016).

[49] H. Salman and D. Maestrini. *Long-range ordering of topological excitations in a two-dimensional superfluid far from equilibrium.* Physical Review A **94**(4) (2016).

[50] S. Kida. *Statistics of the system of line vortices.* Journal of the Physical Society of Japan **39**(5), 1395 (1975).

[51] D. Montgomery and G. Joyce. *Statistical mechanics of ?negative temperature? states.* The Physics of Fluids **17**(6), 1139 (1974).

[52] T. Lundgren and Y. Pointin. *Non-gaussian probability distributions for a vortex fluid.* The Physics of Fluids **20**(3), 356 (1977).

[53] C. A. Jones and P. H. Roberts. *Motions in a bose condensate. IV. axisymmetric solitary waves.* Journal of Physics A: Mathematical and General **15**(8), 2599 (1982).

[54] E. C. Samson, K. E. Wilson, Z. L. Newman, and B. P. Anderson. *Deterministic creation, pinning, and manipulation of quantized vortices in a bose-einstein condensate.* Phys. Rev. A **93**, 023603 (2016).

[55] B. Gertjerenken, P. G. Kevrekidis, R. Carretero-González, and B. P. Anderson. *Generating and manipulating quantized vortices on-demand in a bose-einstein condensate: A numerical study.* Phys. Rev. A **93**, 023604 (2016).

[56] T. Neely, E. Samson, A. Bradley, M. Davis, and B. P. Anderson. *Observation of vortex dipoles in an oblate bose-einstein condensate.* Physical review letters **104**(16), 160401 (2010).

[57] T. Aioi, T. Kadokura, T. Kishimoto, and H. Saito. *Controlled generation and manipulation of vortex dipoles in a bose-einstein condensate.* Physical Review X **1**(2), 021003 (2011).

[58] A. Einstein. *ber einen die erzeugung und verwandlung des lichtes betreffenden heuristischen gesichtspunkt.* Annalen der Physik **322**(6), 132 (1905).

[59] *Quantentheorie der strahlung.* Springer-Lehrbuch Relativistische Quantentheorie pp. 7–118.

[60] G. Labeyrie and R. Kaiser. *Kibble-zurek mechanism in the self-organization of a cold atomic cloud.* Physical Review Letters **117**(27) (2016).

[61] J. Beugnon and N. Navon. *Exploring the kibble-zurek mechanism with homogeneous bose gases.* Journal of Physics B: Atomic, Molecular and Optical Physics **50**(2), 022002 (2017).

[62] G. Gauthier, I. Lenton, N. M. Parry, M. Baker, M. J. Davis, H. Rubinsztein-Dunlop, and T. W. Neely. *Direct imaging of a digital-micromirror device for configurable microscopic optical potentials.* Optica **3**(10), 1136 (2016).

[63] I. Spectrum. *Chip hall of fame: Texas instruments digital micromirror device* (2017).

[64] *Luxbeam 4600 dlp driver board (dlp electronics modules).*

[65] R. Floyd and L. Steinberg. *Anadaptivealgorithm forspatial greyscale.* Proceedings of the Society for Information Display **17**(2), 7577 (1976).

[66] J. Liang, J. R. N. Kohn, M. F. Becker, and D. J. Heinzen. *15% root-mean-square flat-intensity laser beam formed using a binary-amplitude spatial light modulator.* Applied Optics **48**(10), 1955 (2009).

[67] G. R. Dennis, J. J. Hope, and M. T. Johnsson. *Xmds2: Fast, scalable simulation of coupled stochastic partial differential equations.* Computer Physics Communications **184**(1), 201 (2013).